Title
Nonlinear optical properties and spectroscopy of Weyl semimetals

Author
Patankar, Shreyas G

Publication Date
2018

Peer reviewed|Thesis/dissertation

Nonlinear optical properties and spectroscopy of Weyl semimetals

by

Shreyas Patankar

A dissertation submitted in partial satisfaction of the

requirements for the degree of

Doctor of Philosophy

in

Physics

in the

Graduate Division

of the

University of California, Berkeley

Committee in charge:

Professor Joseph W. Orenstein, Chair
Associate Professor James G. Analytis
Professor Daniel S. Rokhsar

Summer 2018

Nonlinear optical properties and spectroscopy of Weyl semimetals

Abstract

Nonlinear optical properties and spectroscopy of Weyl semimetals

by

Shreyas Patankar

Doctor of Philosophy in Physics

University of California, Berkeley

Professor Joseph W. Orenstein, Chair

Nonlinear optical properties of materials are useful both for their practical applications, but also as a characterization tool for symmetry in novel systems. However, the nonlinear optical response of a material is often not as one of its fundamental properties, along with band structure, linear conductivity, etc. This has particularly been the case with the recent interest in "quantum materials": materials such as high-T_c superconductors, topological materials, and exotic magnets. Weyl semimetals are a class of materials where band-touching points have divergent Berry curvature, and are host to a number of unique physical phenomena such as the chiral anomaly and Fermi arc surface states. From the nonlinear optics perspective, Weyl semimetals are interesting since inversion-symmetry breaking Weyl semimetals have been experimentally realized, and breaking of inversion-symmetry is crucial for second order nonlinear optical phenomena.

In this dissertation, I present results from a number of studies of the Weyl semimetal TaAs and related compounds using nonlinear optical techniques. As detailed here, TaAs was discovered to have the largest measured nonlinear optical susceptibility of any material, and further, this susceptibility was found to be caused by a resonance in the spectrum of nonlinear optical conductivity. TaAs was also measured to have a photogalvanic effect that has qualitatively different characteristics depending on the direction of measurement. These nonlinear optical properties of the TaAs family of materials may lead to interesting applications in near-field nonlinear optics, and optical pulse shaping below the diffraction limit.

To my mother, Swati Ganesh Patankar
for raising a scientist

Contents

List of Figures

List of Tables

Acknowledgments

This dissertation marks the culmination of a program through which I was supported by an invaluable network of mentors, collaborators, colleagues, friends, and family. I am thoroughly grateful to my thesis advisor, Prof. Joseph W. Orenstein for taking on the responsibility of my scientific training. Over the long course of my PhD, Joe pushed me further not only in my understanding of Physics, but also the planning, thoughtfulness, discipline, and strategic thinking that is essential in becoming a successful scientist. Among the long list of wonderful collaborators that I've had the pleasure of working with, I would particularly like to thank Prof. J. Steven Dodge, and Prof. Darius Torchinsky for their support and insight at numerous points in my career. I would like to thank Daniel Golubchik, Jamie Hinton, Luyi Yang, and Derek Sahota for teaching me the 101 of being in an optics lab; and Eric Thewalt, Liang Wu, Arielle Little, and Dylan Rees for being the best research team ever, and making the Orenstein lab a fun place to be in every day.

My research productivity would not have been possible without my support network outside of lab. I would like to thank my friend Srijita Kundu for constant, sustained service as my emotional backbone throughout my years in grad school. I would also like to thank my dear friends Andrew Eddins, Victoria Xu, Henoch Wong, Philipp Dumitrescu, Dan Varjas, Harikrishnan Ramani, and Arielle Little for all the best times in Berkeley and beyond. A big part of my graduate school experience was my involvement, first as a delegate, and then as an officer at the UC Berkeley Graduate Assembly (GA). I would like to thank the GA, and the many, many partners within the GA and across the administration and faculty of UC Berkeley for valuable lessons about the university, academia, and the world outside; and specifically call out Dax viviD, Kena Hazelwood-Carter, Linda von Hoene, and Prof. Paul Alivisatos for mentoring me in my leadership journey. And finally, I would like to thank my parents for their dedication.

Chapter 1

Nonlinear optical responses

The study of nonlinear optical properties of materials has been a growing field of study since the advent of lasers, which allowed intense electric fields to interact with materials. Nonlinear optical materials are relevant in the context of important applications such as frequency doubling, optical parametric amplification, and photovoltaic conversion. At the same time, nonlinear optics has also become a vital tool in characterizing new materials, especially for analyzing their symmetry properties.

In this chapter, I outline various principles and concepts that are important for understanding nonlinear optics and how it can be used to study new materials.

1.1 Introduction

how it can be used to study new materials. When an electric field $\vec{E}(t)$ is incident on a material, the material responds with a polarization $\vec{P}(t)$ that can be expressed as a Taylor expansion in powers of the incident field:

$$\frac{P_i(t)}{\epsilon_0} \equiv \int dt' \chi_{ij}^{(1)}(t,t') E_j(t') + \int dt' dt'' \chi_{ijk}^{(2)}(t,t',t'') E_j(t') E_k(t'') + \dots \tag{1.1}$$

in terms of the susceptibility tensors χ of various orders.

The response terms are often discussed in their Fourier version; $\chi_{ij}^{(1)}(\omega)$, $\chi_{ijk}^{(2)}(\omega,\omega',\omega'')$, and so on. The first response tensor $\chi_{ij}^{(1)}$ is the linear susceptibility tensor and can be observed in all materials, and is related to standard linear optical properties such as the dielectric constant ϵ_{ij}, optical conductivity σ_{ij}, and refractive index n_{ij}. A simple model for computing the optical conductivity $\sigma_{ij}(\omega)$ in insulators or dielectric materials is the Lorentz oscillator model that approximates the insulator as a two-level system that interacts with an applied electric field of frequency close to the energy gap. Similarly, in the case of low-

frequency light interacting with metals and systems with free charge carriers, $\sigma_{ij}(\omega)$ can be modeled using Drude's theory of conduction [23].

1.2 Vanderbilt theory of polarization

Static polarization is the response of a material to a constant $\omega = 0$ electric field. In an insulator, an applied electric field causes a displacement in the bound charges leading to local dipole moments. In the standard intuitive picture, also known as the Clausius-Mossotti picture, the local polarization density is defined as the sum of dipole moments inside a unit cell divided by the volume of the unit cell [37] (see figure 1.1). However, under this definition, the value of of the polarization density can be made to have the opposite sign by simply displacing the unit cell by one-half of a lattice parameter.

Experimentally, it is more convenient to define the change in the static polarization induced by an external field as a quantity that can be measured via the net charge transfer. Under the modern theory of polarization developed by Vanderbilt et al. [37, 22], this idea is extended to an intrinsic definition of change in dipole polarization density in a crystal:

$$\Delta\mathbf{P} = \int dt \frac{1}{V_{\text{cell}}} \int_{\text{cell}} d\mathbf{r}\ \mathbf{j}(\mathbf{r}, t) \tag{1.2}$$

that is, the change in polarization density is the instantaneous current density $\mathbf{j}(\mathbf{r}, t)$ integrated over time and the volume of the unit cell.

This definition can be further interpreted in terms of the geometric phase of the wavefunction. Suppose instead of time t, that the electronic wavefunction in the material is changing with respect to an adiabatic parameter λ. The change in the expectation value of the polarization density can be expressed as the expectation value

$$\delta\mathbf{P} = e\langle\psi|\mathbf{x}|\delta\psi\rangle + \text{c.c.}$$

where $\mathbf{x}$ is the position operator. By rewriting the wavefunction $|\psi\rangle$ using the Bloch wavefunctions $u_{n\mathbf{k}}$, we get

$$\mathbf{P}(\lambda) = \frac{ie}{(2\pi)^3}\ \text{Im} \int d\mathbf{k} \sum_n \langle u_{n\mathbf{k}}|\nabla_{\mathbf{k}}|u_{n\mathbf{k}}\rangle \tag{1.3}$$

The quantity $\text{Im} \int d\mathbf{k} \sum_n \langle u_{n\mathbf{k}}|\nabla_{\mathbf{k}}|u_{n\mathbf{k}}\rangle \equiv \mathcal{A}_n$ is known as the Berry connection of the energy level n in the material, and is a geometric property of the wavefunction. Like the static polarization, the Berry connection depends on the choice of gauge in the wavefunction, and hence is not a physically observable quantity. The Berry connection is also only allowed to be non-zero in a material system that brakes time-reversal or inversion symmetry.

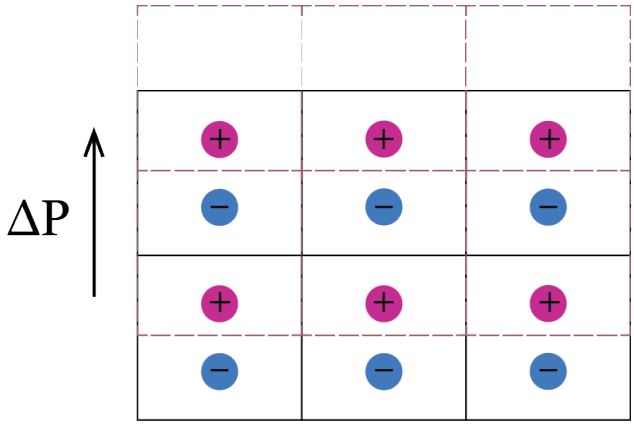

Figure 1.1: Cartoon to illustrate static dipole polarization in a crystalline system. As illustrated by the solid and dashed outlines, the definition of static polarization **P** depends on the choice of the unit cell, and hence is not a well-defined physical observable. The change in static polarization $\Delta\mathbf{P}$, however, is physically well defined and can be measured experimentally.

Ferroelectrics and polar metals

In addition to the static polarization in the presence opf an external electirc field, certain materials have the property that they are able to sustain a net electric polarization in the absence of an external applied electric field. These materials exist in an ordered state in analogy with ferromagnets, and are known as ferroelectric materials. Ferroelectric materials such as $BaTiO_3$ and $LiNbO_3$ are widely used in applications for electro-optic and electronic sensing devices. The existence of ferroelectric order requires the crystal structure of the material to break inversion symmetry, however, not all crystal symmetry groups that break inversion support spontaneous polarization: in addition to breaking inversion, the point group has to have a special "polar direction" along which the polarization can be formed. For example, the $\bar{4}3m$ point group of crystals such as GaAs breaks inversion, but does not pick a polar axis, and hence cannot support ferroelectricity; whereas certain tetragonal and hexagonal groups (4mm, 6mm, etc.) can support a polar axis.

Conventional ferroelectric materials like the ones mentioned above are all insulators. Consider a scenario where unbound charge carriers are introduced into a ferroelectric insulator: the charge carriers will obviously move through the material in order to cancel out the boundary charges and hence eliminate the spontaneous static electric polarization. Such a system will still posses the same symmetry-breaking crystal structure, despite lacking a spontaneous polarization. Materials that have a crystal structure that would support ferroelectricity, but that have a partially filled conduction band allowing for free carriers are known as "Polar metals".

Anderson and Blount showed in 1965 that polar metals can exist [2], and polar metals have recently been a focus of study due to advances in computational techniques that have made it possible to predict materials structures that can host the polar metal state [21].

1.3 Quadratic optical responses

The second term of equation 1.1 with the coefficient $\chi^{(2)}_{ijk}$ is the lowest order *nonlinear* response of the material to the applied electric field, and shall be the focus of study for the remainder of this dissertation. In the frequency domain, this term can be re-written as follows:

$$P^{(2)}_i(\omega) = \epsilon_0 \, \chi^{(2)}_{ijk}(\omega, \omega', \omega'') E_j(\omega') E_k(\omega''). \tag{1.4}$$

There are two special cases of equation 1.4 that are usually highlighted for attention; namely the case satisfying $\omega = \omega' + \omega''$ known as *sum frequency generation* and the case satisfying $\omega = \omega' - \omega''$ known as *difference frequency generation*. Further, when the incident electric field is nearly monochromatic with a center frequency of ω, we have the scenario of *second harmonic generation* described by:

$$P^{\text{shg}}_i(2\omega) = \epsilon_0 \, \chi^{\text{shg}}_{ijk}(2\omega, \omega, \omega) E_j(\omega) E_k(\omega) \tag{1.5}$$

in which case, the susceptibility $\chi^{\text{shg}}_{ijk}(2\omega, \omega, \omega)$ can be expressed simply as $\chi^{\text{shg}}_{ijk}(\omega)$. Difference frequency generation in the truly monochromatic case, where $\omega' = \omega''$ results in various $\omega = 0$ effects which we shall not discuss here. However, all the experiments described in the following chapters were performed with incident light from pulsed lasers which have a finite frequency distribution $\Delta\omega$. For typical pulsed lasers with center wavelength around 800 nm or energy around 1.55 eV, the spread in the frequency distribution is approximately 1-10 THz or 4-40 meV in energy units. The difference frequency generation under these conditions corresponds to a number of physical phenomena such as optical rectification and photogalvanic effects. A simplified description of these can be expressed as:

$$P^{\text{dfg}}_i(\Delta\omega) = \epsilon_0 \, \chi^{\text{dfg}}_{ijk}(\Delta\omega, \omega, \omega + \Delta\omega) E_j(\omega) E_k(\omega + \Delta\omega) \tag{1.6}$$

where as before, the shortened notation $\chi^{\text{dfg}}_{ijk}(\Delta\omega, \omega, \omega + \Delta\omega)$ can be used.

As in the linear case, the nonlinear optical susceptibility $\chi^{(2)}_{ijk}$ is related to the nonlinear conductivity $\sigma^{(2)}_{ijk}$, the latter of which is often more relevant from the perspective of theoretical calculations and simulations. In addition, while the conventional theoretical technique to calculate the quadratic optical properties relied on second order perturbation theory, recent work has demonstrated the relationship between the quadratic optical properties and properties of the electronic wavefunction such as the Berry connection $\mathcal{A}_n$ [31].

1.4 Outline

The remainder of this dissertation is a discussion of various techniques used to study the curious $\chi^{(2)}$ and $\sigma^{(2)}$ responses in a family of materials known as Weyl semimetals. Chapter 2 provides a brief introduction to Weyl semimetals and their importance in physics, and describes the experiments used to measure anomalously large and anisotropic second harmonic generation in these materials. Chapter 3 focuses on the difference frequency term $P_i(\Delta\omega)$ along with the experimental technique of terahertz emission spectroscopy (TES) used in its measurement. Chapter 4 expands on the giant second harmonic generation from chapter 2, by studying the response with incident light frequencies in the near- and mid-infrared regions of the spectrum, and also describes the discovery of a new theorem that relates nonlinear optical properties to gauge-invariant cumulants of the electronic charge distribution. Finally, chapter 5 discusses potential impacts and applications of the discovery of anomalous nonlinear optical properties in these materials.

Chapter 2

Giant second harmonic generation in TaAs

2.1 Weyl semimetals

Weyl semimetals are a newly discovered class of materials with non-trivial band structure geometry [48, 28, 18]. Most notably, the band structure of these materials contains "band-touching" points which correspond to a divergence of the Berry curvature. They are known to host a number of exotic physical phenomena, such as topologically protected "Fermi arc" edge states [49] and the Chiral anomaly [51].

A key characteristic requirment for materials that host these states is that they have

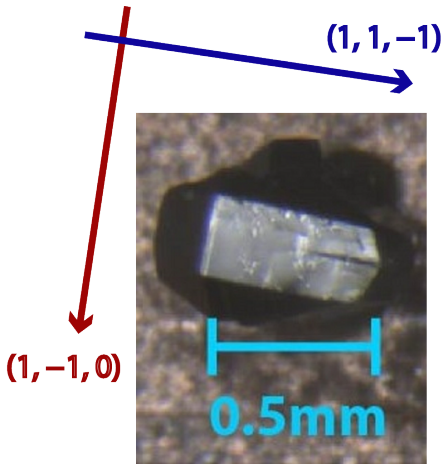

Figure 2.1: A single crystal of TaAs showing the ⟨112⟩ face. The in-plane axes that contain a component of the polar axis, and perpendicular to the polar axis, $(1, 1, -1)$ and $(1, -1, 0)$ respectively, are highlighted.

to break either time reversal or inversion symmetry. Weyl semimetal materials that break time reversal symmetry have yet to be observed in experiments, although they have been predicted to exist in classes of materials such as the magnetic Heusler alloys [45]. On the other hand, inversion breaking Weyl semimetals have been realized in a number of materials systems, most famously in the TaAs family of materials, also known as the transition metal monopnictides [27]. This family of materials has a polar point group symmetry, that is, they possess a polar axis along which mirror symmetry is broken. As mentioned in Chapter 1, the inversion breaking Weyl semimetals hence also belong to the rare category of polar metals.

Large single crystals of TaAs up to 2mm in linear dimensions can be grown using chemical vapor transport (CVT), using Iodine as a transport agent. Vapor transport grown CVT crystals have naturally grown facets along the $\langle 001 \rangle$, $\langle 101 \rangle$, and $\langle 112 \rangle$ crystalline directions. Of these, the $\langle 001 \rangle$ face has the polar axis normal to the plane, and hence is not expected to display any second harmonic response. The $\langle 101 \rangle$ and $\langle 112 \rangle$ faces both have an in-plane component of the polar axis. The measurements described here were performed on the $\langle 112 \rangle$ face (see figure 2.1), where it is useful to identify the in plane direction that have a component of the polar axis and are perpendicular to the polar axis: $(1, 1, -1)$ and $(1, -1, 0)$ respectively.

2.2 Polarimetry of SHG

Given that $\chi^{(2)}_{ijk}$ is a third rank tensor, a full characterization of the nonlinear optical susceptibility has to depend strongly on the polarization states of the incident first harmonic, and the radiated second harmonic light.

Fig. 2.2 shows a schematic of the optical apparatus used to study the polarization dependence of second harmonic generation in various nonlinear materials. The intensity of the second harmonic light depends quadratically on that on the incident first harmonic, and hence, there is a significant benefit to using light sources with large instantaneous electric fields to induce SHG. For this reason, the fundamental harmonic light sources used in the apparatus were pulsed femtosecond lasers. Specifically, the two lasers used for data acquisition in this experiment were the Coherent® Mantis™ Ti:Sapphire oscillator providing 50fs pulses at 800nm with an average power of 200mW at an 80 MHz repetition rate; and the Toptica® FFPro-NIR™ Er:Fiber laser providing 100fs pulses at 800nm with an average power of 150mW at an 80 MHz repetition rate.

A series of reflective neutral-density filters were subsequently used to control the intensity of the light incident on the sample. Depending on the exact application, the neutral density filters were chosen so as to have the final intensity incident on the sample be lower than 10mW. To suppress $1/f$-noise from the laser source, the incident light beam is chopped at approximately 1 kHz. To control the incident polarization state, a polarizer is used to

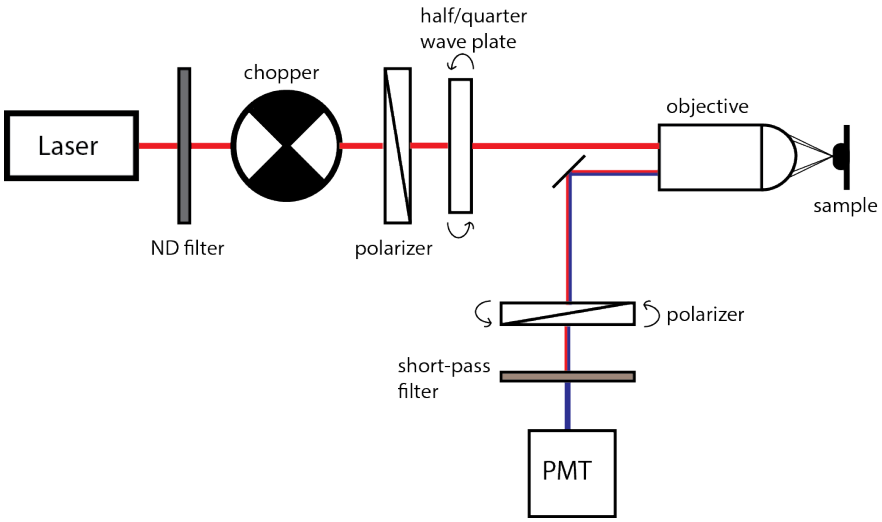

Figure 2.2: Schematic of the experimental apparatus used to study polarization dependence of second harmonic generation in a sample.

"clean" the polarization state generated by the laser. A zero-order halfwave plate is then used to rotate the polarization to a desired angle. The laser beam is focused onto the sample using an Olympus PLAN 10X microscope objective to a spot size that is approximately 10 μm wide.

In reflection geometry, the intensity of the generated SHG light is too low to be observed using common laboratory aids. The optics for the generated second harmonic light are aligned using the fact that the second harmonic radiation co-propagates with the specular reflection of the incident first harmonic light. Since the objective has a relatively large numerical aperture of 0.25, it is possible to use infrared cards and viewers to ensure that the reflected (and hence second harmonic) light is in fact collected and re-collimated by the microscope objective. The path of propagation for the second harmonic beam can be physically separated from that of the incident light by using either a 50-50 beamsplitter or a carefully positioned D-mirror. Although the alignment procedure with a beamsplitter is more convenient, a D-mirror is more likely to preserve polarization states, and is hence used for the polarimetry measurements.

A linear polarizer, labeled "analyzer" is used to measure the SHG intensity along the desired polarization angle. For precision and in order to automate the process, the initial half-wave plate and the final analyzer are mounted on identical high-speed motorized rotation stages, with the halfwave plate always set to move 1/2 the angular displacement as the analyzer. Finally a set of two band-pass filters centered at 400nm were used to isolate the SHG light from the specular reflection of the first harmonic light prior to detection.

Detectors for SHG

With the exception of transparent nonlinear materials with carefully selected phase-matching conditions [42], the intensity of SHG radiation from most samples is orders of magnitude lower than the incident intensity. Thus, SHG measurements often have to rely on photodetectors that are more sensitive than conventional semiconductor photodiodes. The SHG polarimetry measurements described here used a Thorlabs® PMM02 multi-alkali photomultiplier tube (PMT), with a built in voltage amplifier. PMTs are highly sensitive detectors and can be easily overwhelmed by ambient room light. For this reason, the PMT used in the SHG experiment was housed in a specially built dark enclosure. The PMM02 has a variable gain control which was set so as to provide a gain of approximately 10^5 in signal. Data was acquired using a Zurich Instruments® MFLI™ lock-in amplifier that was synchronized with the mechanical chopper. The MFLI also provided the control voltage signal needed to control the gain on the photomultiplier tube.

2.3 $\chi^{(2)}$ tensor components

The radiated second harmonic intensity were measured in a series of polarization configurations or channels, with the direction 0^o defined as being normal to the plane of the optical bench.

1. *Parallel*: The incident polarization direction and the final analyzer direction are rotated starting from the 0^0 by 360^o while being constantly parallel to each other. This is analogous to Holding the polarizers parallel but stationary, and rotating the sample by 360^o.

2. *Perpendicular*: The incident polarization direction and the final analyzer direction are rotated starting from 0^0 by 360^o while being constantly perpendicular to each other. This is analogous to Holding the polarizers parallel but stationary, and rotating the sample by 360^o.

3. *Vertical*: The analyzer direction is held constant at 0^0 while the initial polarization direction is rotated starting from 0^0 by 360^o.

4. *Horizontal*: The analyzer direction is held constant at 90^0 while the initial polarization direction is rotated starting from 0^0 by 360^o.

Fig. 2.3a shows the intensity of the SHG light as a function of the angle of the incident linear polarization in the *parallel* channel. The polar pattern is observed to be highly anisotropic, picking out a special direction. We identify this direction as being the in-plane component (1,1,1) of the crystalline polar axis (0,0,1), and then use this information to align the sample so that the $(1, 1, -1)$ direction is along the 0^o direction of the laboratory frame of reference. This alignment is essential for accurate measurement and analysis of the signal in

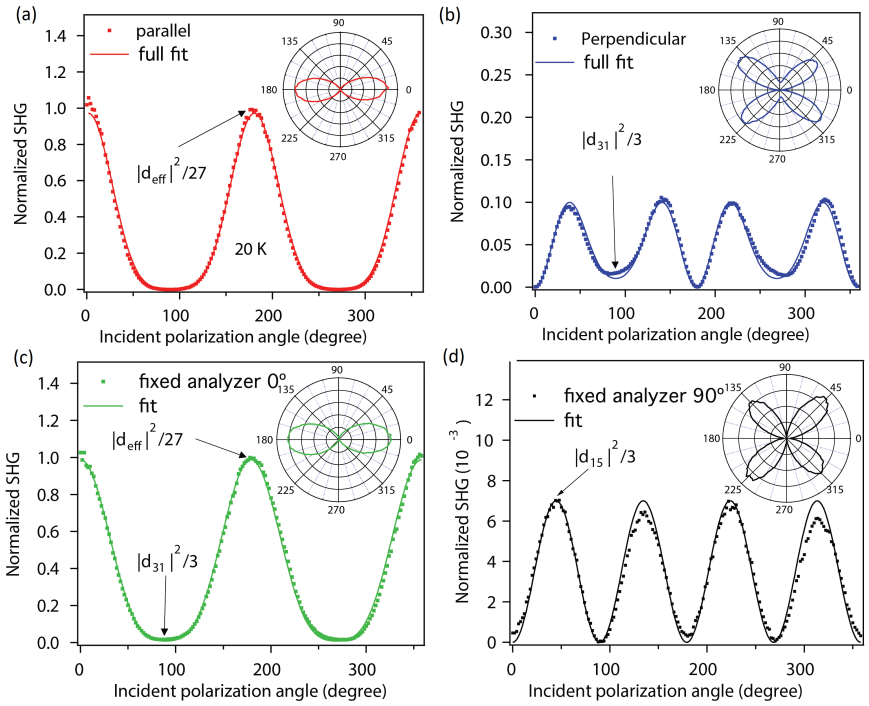

Figure 2.3: Dependence of the SHG intensity as a function of the incident polarization angle in various polarization "channels". All data is normalized so that the peak signal in the parallel channel is equal to 1. The fits to the data are according to the functions described in the text. Figures reproduced from Wu et al., (2017) [46]

the *vertical* and *horizontal* channels. Fig. 2.3b shows the SHG intensity in the *perpendicular* channel, and Fig. 2.3c, d respectively show the *vertical* and *horizontal* channels.

To calculate the components of the third rank susceptibility tensor $\chi^{(2)}$ from the measured data, we reproduce the procedure outlined in ref. [35]. We start with the relation defining the second harmonic susceptibility in terms of the electric fields of the incident $\mathbf{E}^{1\omega}$ and radiated $\mathbf{E}^{2\omega}$ fields:

$$E_i^{2\omega} = \chi_{ijk}^{\text{shg}} E_j^{1\omega} E_k^{1\omega}, \tag{2.1}$$

where a sum over repeated indices is implied. We use the notation $\hat{x}, \hat{y}, \hat{z}$, to correspond to the crystalline axes $(1,0,0)$, $(0,1,0)$, $(0,0,1)$. The crystal structure of TaAs corresponds to the point group $4mm$, which allows only three distinct components of the χ_{ijk} tensor: χ_{zzz}; $\chi_{zxx} = \chi_{zyy}$; $\chi_{xxz} = \chi_{xzx} = \chi_{yyz} = \chi_{yzy}$.

It is useful to label the in-plane component of the polar axis $(1,1,-1)$ as the axis "γ", and correspondingly label the perpendicular in-plane direction $(-1,1,0)$ as the axis "α". If the incident light has intensity I_0, with linearly polarized electric field expressed by $\mathbf{E}^{1\omega} =$

$\sqrt{I_0}\,(\hat{\alpha}\sin\theta + \hat{\gamma}\cos\theta)$, in the parallel channel, the intensity can be expressed in terms of the angle θ of the incident polarization state with respect to the "γ" axis:

$$\begin{aligned} I_{\text{para}}(\theta) &= \left|E_\alpha^{2\omega}\sin\theta + E_\gamma^{2\omega}\cos\theta\right|^2 \\ &= \left|\frac{1}{\sqrt{2}}\left(-E_x^{2\omega} + E_y^{2\omega}\right)\sin\theta + \frac{1}{\sqrt{3}}\left(E_x^{2\omega} + E_y^{2\omega} - E_z^{2\omega}\right)\cos\theta\right|^2. \end{aligned}$$

We wish to express this in terms of the tunable quantities $E_z^{1\omega} = -\frac{E_\gamma^{1\omega}}{\sqrt{3}}$ and $E_\gamma^{1\omega} = \sqrt{I_0}\cos\theta$. To do this, we first expand $\mathbf{E}^{2\omega}$ in terms of $\mathbf{E}^{1\omega}$ via

$$E_x^{2\omega} = 2\chi_{xxz}E_x^{1\omega}E_z^{1\omega}, \qquad E_y^{2\omega} = 2\chi_{yyz}E_y^{1\omega}E_z^{1\omega}, \qquad E_z^{2\omega} = \chi_{zxx}\left(E_x^{1\omega}\right)^2 + \chi_{zyy}\left(E_y^{1\omega}\right)^2 + \chi_{zzz}\left(E_z^{1\omega}\right)^2, \tag{2.2}$$

and transform back from the xyz to the $\alpha\gamma$ basis via

$$E_x^{1\omega} = -\frac{E_\alpha^{1\omega}}{\sqrt{2}} + \frac{E_\gamma^{1\omega}}{\sqrt{3}}, \qquad E_y^{1\omega} = \frac{E_\alpha^{1\omega}}{\sqrt{2}} + \frac{E_\gamma^{1\omega}}{\sqrt{3}}, \qquad E_z^{1\omega} = -\frac{E_\gamma^{1\omega}}{\sqrt{3}}. \tag{2.3}$$

This yields

$$\begin{aligned} I_{\text{para}}(\theta) &= \frac{I_0^2}{3}\left|\chi_{xxz}\cos\theta\sin^2\theta + \left(\frac{4}{3}\chi_{xxz}\cos^2\theta + \chi_{zxx}\left(\sin^2\theta + \frac{2}{3}\cos^2\theta\right) + \frac{1}{3}\chi_{zzz}\cos^2\theta\right)\cos\theta\right|^2 \\ &= \frac{I_0^2}{27}\left|3\chi_{xxz}\cos\theta\sin^2\theta + \left(4\chi_{xxz}\cos^2\theta + \chi_{zxx}\left(3\sin^2\theta + 2\cos^2\theta\right) + \chi_{zzz}\cos^2\theta\right)\cos\theta\right|^2 \\ &= \frac{I_0^2}{27}\left|(6\chi_{xxz} + 3\chi_{zxx})\cos\theta\sin^2\theta + (4\chi_{xxz} + 2\chi_{zxx} + \chi_{zzz})\cos^3\theta\right|^2. \end{aligned}$$

We define $\chi_{\text{eff}} = \chi_{zzz} + 2\chi_{zxx} + 4\chi_{xxz}$, which gives us the expression,

$$I_{\text{para}} = \frac{I_0^2}{27}\left|3(2\chi_{xxz} + \chi_{zxx})\cos\theta\sin^2\theta + \chi_{\text{eff}}\cos^3\theta\right|^2. \tag{2.4}$$

We can similarly obtain expressions for the other three channels:

$$I_{\text{perp}} = \frac{I_0^2}{27}\left|3\chi_{zxx}\sin^3\theta + (\chi_{\text{zzz}} + 2\chi_{\text{zxx}} - 2\chi_{\text{xzx}})\cos^2\theta\sin\theta\right|^2, \tag{2.5}$$

$$I_{\text{vertical}}(\theta) = \left|E_3^{2\omega}\right|^2 = \left|\frac{1}{\sqrt{3}}\left(E_x^{2\omega} + E_y^{2\omega} - E_z^{2\omega}\right)\right|^2 = \frac{1}{27}\left(3\chi_{zxx}\sin^2\theta + \chi_{\text{eff}}\cos^2\theta\right), \tag{2.6}$$

and

$$I_{\text{horiz}}(\theta) = \left|E_\alpha^{2\omega}\right|^2 = \left|\frac{1}{\sqrt{2}}\left(-E_x^{2\omega} + E_y^{2\omega}\right)\right|^2 = \frac{1}{3}I_0^2|\chi_{xxz}|^2\ \sin 2\theta. \tag{2.7}$$

As an initial step, we can use these functions as fits to the data in the various channels to extract the $\chi^{(2)}$ components in normalized units, as shown in figure 2.3. That is, these data sets allow us to calculate the relative magnitudes of the tensor components $\frac{|\chi_{\mathrm{zxx}}|}{|\chi_{\mathrm{eff}}|} \approx 0.01$ and $\frac{|\chi_{\mathrm{xzx}}|}{|\chi_{\mathrm{eff}}|} \approx 0.04$ at room temperature. Since these ratios are both much smaller than 1, we observe that The SHG tensor response of TaAs is almost entirely dominated by a single component, χ_{zzz}, and hence, is highly anisotropic.

2.4 Benchmarking

The nonlinear susceptibility $\chi^{(2)}$ is a dimensionful quantity that has dimensions of inverse electric field (m/V) in SI units. In fact, as an exercise in dimensional analysis, one can use a typical length scale comparable to a unit cell of 1-10 Å and a typical band structure energy scale of 10 eV to estimate that a typical value of $|\chi^{(2)}|$ can be expected to be around 100 pm/V.

However, for a more formal calculation, we compare the SHG signal from TaAs with that from GaAs and ZnTe, materials whose nonlinear optical properties have previously been well characterized [5, 44]. GaAs and ZnTe have a relatively large nonlinear SHG response, and both have a crystal structure $\bar{4}$3m that has only a single symmetry-allowed tensor component: χ_{xyz}. The samples used for benchmarking the response from TaAs were a single crystal of GaAs showing the [1,1,1] face, and a single crystal of ZnTe showing the [1,1,0] face. Figure 2.4a,b,c show the SHG intensities from TaAs, ZnTe, and GaAs, all plotted on a scale where the maximum signal in the TaAs parallel channel is set to 1. We can see immediately that to plot the data from all three materials on the same scale, the signals from ZnTe and TaAs have to be multiplied by factors of 4 and 6.6 respectively. This suggests that the SHG response of TaAs is significantly larger than that from either ZnTe or GaAs. To calculate the $\chi^{(2)}$ values directly, we fit the data with the following functions:

For the [1,1,0] facet of ZnTe, the SHG intensity in the two channels is given by

$$I_{\mathrm{parallel}} = 9I_0^2 \left|\chi_{xyz}\right|^2 \cos^4\theta \sin^2\theta, \tag{2.8}$$

and

$$I_{\mathrm{perp}} = I_0^2 \left|\chi_{xyz}\right|^2 (2\cos\theta \sin^2\theta - \cos^3\theta)^2. \tag{2.9}$$

whereas for the [1,1,1] facet of GaAs, they are

$$I_{\mathrm{parallel}} = \frac{2}{3} I_0^2 \left|\chi_{xyz}\right|^2 (\cos^3\theta - 3\cos\theta \sin^2\theta)^2, \tag{2.10}$$

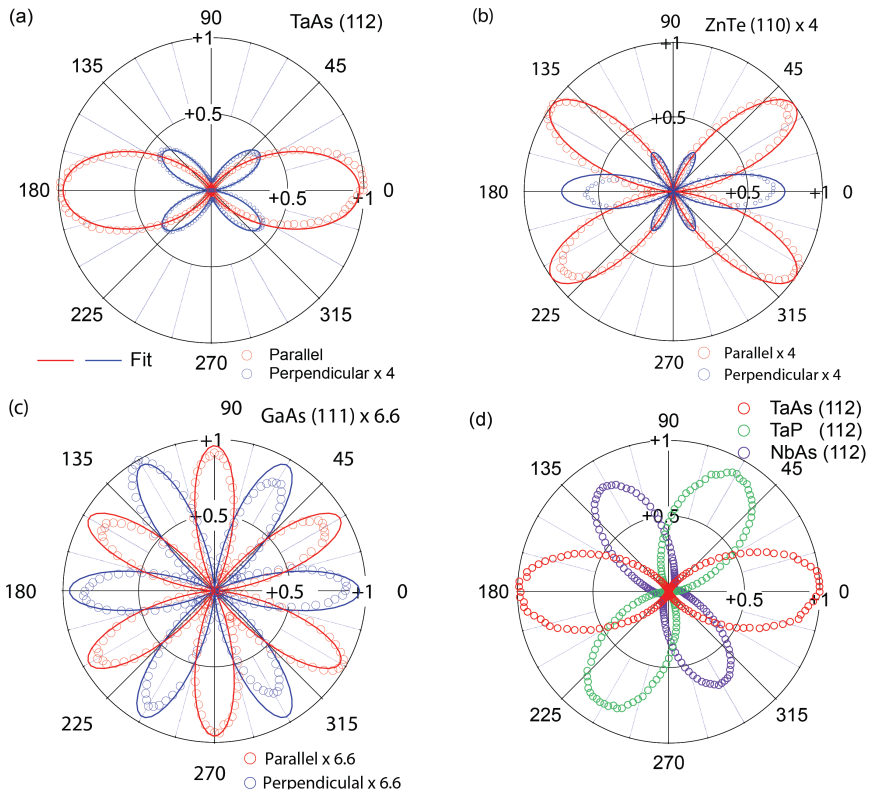

Figure 2.4: Benchmarking the SHG signal from various materials, all plotted on the same scale, normalized such that the maximum in the first panel is 1. (a) SHG signal from TaAs in the *parallel* and *perpendicular* channels, with the latter multiplied by a factor of 4 for easier visibility. (b) SHG signal from a [1,1,0] facet of ZnTe in the *parallel* and *perpendicular* channels, both multiplied by a factor of 4 for easier visibility. (c) SHG signal from a [1,1,1] facet of GaAs in the *parallel* and *perpendicular* channels, both multiplied by a factor of 6.6 for easier visibility. (d) SHG signal from $\langle 112 \rangle$ facets of TaAs, NbAs, TaP in the *parallel* channels. The data from TaP and NbAs are rotated by 60^o and 120^o for easier visibility. Figures reproduced from Wu et al., (2017) [46]

and

$$I_{\text{perp}} = \frac{2}{3} I_0^2 \left|\chi_{xyz}\right|^2 (\sin^3\theta - 3\cos^2\theta \sin\theta)^2. \tag{2.11}$$

In order to accurately compare the SHG intensity from various materials, we need to account for correction factors arising from linear optical properties (such as refractive index and Fresnel coefficients). The nonlinear susceptibility relevant to the experimental set up described here can be labeled as the "reflection" susceptibility $\chi_R^{(2)}$, and can be related to the "intrinsic" susceptibility $\chi_I^{(2)}$ through the formula described by Bloembergen and Pershan [6]:

$$\chi_R^{(2)} = \frac{\chi_I^{(2)}}{\left(\sqrt{\epsilon(2\omega)} + \sqrt{\epsilon(\omega)}\right)\left(\sqrt{\epsilon(2\omega)} + 1\right)} T(\omega)^2 \tag{2.12}$$

where $\epsilon(\omega)$ is the complex, frequency dependent dielectric constant of the material, and $T(\omega)$ is the transmission coefficient which can be expressed in terms of the refractive index $n(\omega)$ as $T(\omega) = \dfrac{2}{1+n(\omega)}$

Material	χ_{ijk} component	$\lvert\chi\rvert$ (pm/V)	Incident light	Ref.
TaAs	χ_{zzz}	3600 ($\pm$550)	800nm	[46]
GaAs	χ_{xyz}	350	810nm	[5]
ZnTe	χ_{xyz}	250, 450	800nm, 700nm	[44]
$BaTiO_3$	χ_{zzz}	15	900nm	[30]
$BiFeO_3$	χ_{zzz}	15-19	1550nm, 800nm	[15, 20]
$LiNbO_3$	χ_{zzz}	26	852nm	[40]
$PbTiO_3$	χ_{zzz}	200	150nm	[50]

Table 2.1: Nonlinear optical susceptibility $\chi^{(2)}$ of various materials that have been studied either experimentally or theoretically, at various wavelengths of incident light. The uncertainty in the value for TaAs is determined by varying the complex phase between χ_{zzz} and χ_{xzx}.

Fitting the data to these functions, and after applying the Bloembergen-Pershan correction, we can obtain the ratio of the amplitudes of $\chi_{\text{eff}}^{\text{TaAs}} \approx \chi_{zzz}^{\text{TaAs}}$ and χ_{xyz}^{ZnTe}, χ_{xyz}^{GaAs}; and then use the published values for ZnTe, GaAs to obtain a numerical value for the nonlinear optical susceptibility of TaAs. Table 2.1 shows this calculated value for the χ_{zzz} component of the nonlinear optical susceptibility of TaAs, and compares it with that of GaAs and ZnTe, as

well as a number of other known nonlinear optical materials. We observe that the nonlinear optical susceptibility of TaAs is not only higher than that of GaAs and ZnTe, but is in fact nearly 10 times larger than the largest nonlinear optical susceptibility previously measured. In addition, as shown in figure 2.4d, the SHG response from other materials in the TaAs family, namely NbAs, and TaP, are comparable to that from TaAs, and hence these materials also have a large anisotropic nonlinear optical response.

The relationship between the anomalously large nonlinear optical susceptibility of the transition metal monopnictide family, and the properties related to the Weyl physics in these materials (such as the divergent Berry curvature), are not immediately evident. This result motivates further study into ab-initio calculations of nonlinear optical properties of materials, particularly in systems with topologically nontrivial band structures. A minimal model calculation based on the shift vector formalism for nonlinear optics suggests that the dominant component of the nonlinear optical susceptibility $\chi^{(2)}_{zzz}$ is related to the expression $|v_{z,12}(\mathbf{k})|^2 R_{z,12}(\mathbf{k})$, integrated over all values of $\mathbf{k}$ in the Brillouin zone, where $|1\rangle$ and $|2\rangle$ are two non-degenerate energy states in the minimal model [46]. In the Weyl semimetal TMMPs, we may interpret that the striking amplitude of the nonlinear optical susceptibility is possibly related to the divergent Berry curvature at nodal points in the band structure. However, such proof is only possible when the photon energy is lower than the Lifshitz energy ($\sim$ 50 meV), where nonlinear optical responses are related with Weyl quasiparticles dominantly.

As shall be shown in Chapter 4, further insight into the origin of the giant anisotropic second harmonic generation is obtained by studying the spectrum of the $\chi^{(2)}$ as a function of incident photon wavelength, by varying it from 800 nm to 2500 nm.

Chapter 3

Terahertz generation and photogalvanic effects

3.1 Introduction

Photogeneration of current in semiconductors in which inversion symmetry is broken by doping-induced gradients of chemical potential is currently the basis of photovoltaic energy conversion and photodetection technologies. However, photocurrent in crystals in which inversion-symmetry is intrinsically broken, such as ferroelectrics, have been receiving increasing attention for photovoltaic applications. As described in a previous chapter, a new class of *metallic* inversion breaking compounds are under intense investigation as examples of Weyl semimetals – crystals whose space group allows non-degenerate bands to cross at isolated points in momentum space, creating a linear dispersion relation analogous to relativistic chiral fermions. To date, the best characterized of this class of materials are the transition metal monopnictides (TMPs) – polar metals whose symmetry would allow ferroelectricity, but are metallic instead. We have already established that the materials have a giant optical second harmonic response [46], and offer new opportunities in the search for materials with large photocurrent response.

Theoretical studies have proposed a number of microscopic mechanisms for photogalvanic effects both in Weyl semimetals, and more generally in inversion-symmetry breaking materials. These include effects such as *optical rectification* which refers to nonlinear, non-resonant intraband excitation of photocurrents [41], *shift current* caused by a displacement of the real space Wannier functions between conduction and valence bands [50, 31], and injection current which arises from the difference in the band velocity of initial and photoexcited states [7]. Optical rectification is a commonly observed phenomenon in semiconductor crystals lacking a center of inversion [11], and shift and injection currents have been observed in a variety of material systems including wurtzite semiconductors [26], and topological insulator surface states [7]. Optical rectification, shift current, and injection current can all be

described as coherent photogalvanic effects, since the time scale of their onset is the coherence time of the excited states. Alternative, incoherent mechanisms of photogalvanic effects were proposed by Belinicher et al. [4, 3], where the photocurrent generation timescale can depend on extrinsic parameters such as the electron scattering rate. However, these effects have since received little theoretical attention since, although it has recently been shown that incoherent mechanisms are in fact expected to dominate other mechanisms in the presence of impurity scattering [25].

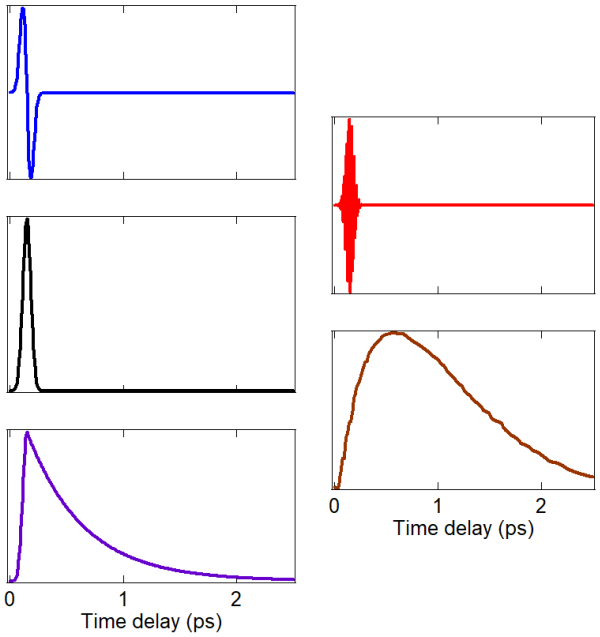

Figure 3.1: Schematic time dependence of coherent and incoherent photogalvanic effects when induced by an ultrashort laser pulse. Counterclockwise from top right: (a) The electric field of the stimulating laser pulse, (b) optical rectification, (c) shift current, (d) injection current, (d) incoherent current

This chapter presents the dynamics of photocurrent generation in the Weyl semimetal, TaAs, using terahertz emission spectroscopy (TES) [7, 16]. In this technique, samples are photoexcited with ultrashort laser pulses and the resulting photocurrent transient radiates an electromagnetic pulse that is detected in the far field by electro-optic sampling. The sub-picosecond temporal resolution afforded by electro-optic sampling provides us with an additional distinguishing parameter between the various photogalvanic effects [26], namely, the time dependence of the photocurrent (see schematic in Figure3.1). TES has an additional advantage over conventional *dc* measurements of photocurrent of eliminating the need for precisely aligned electrical contacts with the samples, which are responsible for artefact signals arising from photothermal effects [29]. Exploiting the advantages of TES allows the ability to determine the dominant mechanism for photocurrent generation in TaAs. As shall

be shown below, photocurrents in TaAs are generated by two distinct mechanisms: photocurrents parallel to the polar axis are generated by an incoherent process, while photocurrents perpendicular to the polar direction are generated by an incoherent process.

3.2 Terahertz emission spectroscopy

Figure 3.2(a) shows a schematic of the apparatus that was used to to detect photocurrents induced in TaAs. In order to generate an adequately intense terahertz electric fields, the nonlinear optical samples are stimulated by amplified laser pulses, generated by a Coherent® regenerative amplifier operating at a repetition rate of 250 kHz. Ultrafast laser pulses of duration 100fs, energy 3μJ, and center wavelength 800nm, are incident on the sample to be studied. Any photocurrent induced in the sample may generate a time-dependent electric field, which is then collected using off-axis paraboloid mirrors (OAPs) and focused on to a ZnTe crystal, where it is detected through electro-optic sampling [43, 33]. The laser pulses are incident normal to the surface of the sample, and likewise, the emitted electric field is measured propagating normal to the sample surface.

Bandwidth calibration

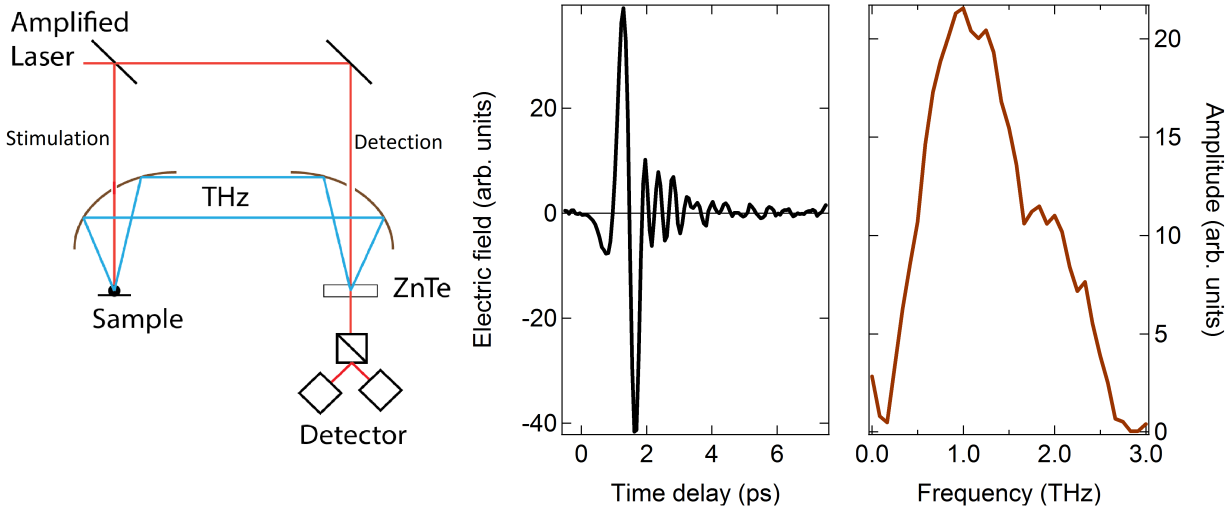

Figure 3.2: (a) Schematic of the experimental apparatus. (b) Measurement of electric field generated by laser pulses incident on ZnTe surface, as a function of time delay between the generation and detection laser pulses. (c) Fourier transform of signal in (b), showing non-zero signal in the frequency domain for frequencies between 0.2 and 3.0 THz.

To calibrate the bandwidth of the response from our detection system, we placed a crystal of ZnTe in the position of the sample, with the laser pulses incident normal to the [110] face.

The generation of a photocurrent proportional the intensity of incident light is an example of second-order nonlinear process. The photocurrent transient generated by a laser pulse is most simply expressed through its Fourier transform, $\mathbf{J}(\omega)$, which is given by,

$$\mathbf{J}(\omega_1 - \omega_2) = \sigma^{(2)}(\omega_1, \omega_2)\mathbf{E}(\omega_1)\mathbf{E}(\omega_2) \tag{3.1}$$

Since the incident electric field consists of laser pulses that are centered around frequency ω but have a small spread in frequency $\Delta\omega$, the resultant polarization will vary with a characteristic frequency of the variation $\Delta\omega$.

$$P_i^{(2)}(\Delta\omega) = \chi_{ijk}^{(2)} E_j(\omega) E_k(\omega + \Delta\omega) \tag{3.2}$$

The frequency spread $\Delta\omega$ is Fourier-limited by the pulse width of our laser. The frequency spread in $\vec{P}(\Delta\omega)$, and hence $\vec{J}(\Delta\omega)$ is significantly broader than the detection bandwidth of our apparatus, and hence the bandwidth of terahertz radiation from ZnTe is thus determined by the pulse width of the incident laser pulses and by phonon absorption in ZnTe. Figure 3.2b shows the amplitude of the electric field radiated by ZnTe as a function of time delay between the generation and detection laser pulses. Figure 3.2c shows the Fourier transform of the time domain signal. The experimental apparatus has a measurable response in the frequency domain for radiation with frequencies between 0.2 and 3.0 THz.

Geometry of the measurement

Recall from Chapter 2 that the morphology of as grown crystals of TaAs most commonly exhibits facets normal to the $\langle 001 \rangle$, $\langle 101 \rangle$, and $\langle 112 \rangle$ directions [27]. Of these, the $\langle 001 \rangle$ facet is normal to the polar axis, and as such is not expected to have a second order response to normally incident radiation. Figure 3.3b and 3.3c show respectively, a schematic of the $\langle 101 \rangle$ and $\langle 112 \rangle$ crystal facets. In both facets, polarization-resolved second harmonic generation [46] is used to identify in-plane axes that are perpendicular to the polar axis ($(0, 1, 0)$ and $(1, -1, 0)$), and that contain the in-plane component of the polar axis ($(1, 0, -1)$ and $(1, 1, -1)$). Henceforward, these are referred to as the in-plane *non-polar* and *polar* directions, respectively. The TES experiment was performed on two faces: (a) $\langle 101 \rangle$, i.e. the direction of propagation of both the incident laser pulses and the stimulated terahertz radiation are normal to the $\langle 101 \rangle$ plane, and (b) $\langle 112 \rangle$, i.e. the direction of propagation of both the incident laser pulses and the stimulated terahertz radiation are normal to the $\langle 112 \rangle$ plane. For either facet, the radiated electric field was measured with polarization either along the polar or the non-polar directions.

3.3 PGE along non-polar direction

Figure 3.4a shows the electric field emitted parallel to the non-polar direction, with the experiment being performed on the $\langle 112 \rangle$ face of a TaAs crystal (see Methods for details).

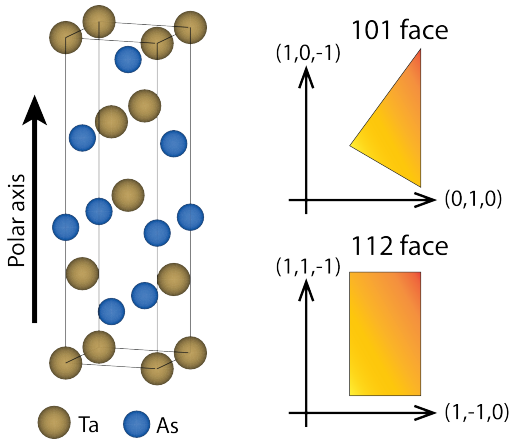

Figure 3.3: (a) Crystal structure of TaAs showing the $4mm$ point group. The c-axis represents the polar direction of the crystal. As grown TaAs crystals have three faces: (b) $\langle 101 \rangle$, (c) $\langle 112 \rangle$, and (not shown) $\langle 001 \rangle$. Within the plane of the crystal faces $\langle 101 \rangle$, $\langle 112 \rangle$, we have identified the directions that contain a component of the polar direction (namely, $(1, 0, -1)$ and $(1, 1, -1)$) and the directions that are perpendicular to the polar direction (namely, $(0, 1, 0)$ and $(1, -1, 0)$). The $\langle 001 \rangle$ face does not have an in-plane component of the polar axis, and as such is not expected to have the photogalvanic effect.

The emitted electric field parallel to the $(0, 1, 0)$ direction was observed to be almost zero when the incident laser polarization state is parallel to either $(1, 0, -1)$ or $(0, 1, 0)$, but that it has an equal and opposite magnitude when the incident laser polarization is either left or right circular. The difference between the electric field radiated with left and right circularly polarized radiation is referred to as the circular dichroism. We also measure the electric field emitted with polarization parallel to the non-polar direction, but stimulated by linearly polarized incident laser pulses. While the electric field signal is indistinguishable from the background when the incident laser polarization is at either 0^{o} or 90^{o} to the polar axis, we see a measurable signal when the incident laser polarization is at $\pm 45^{o}$ (Figure 3.4b) Note that the temporal profile of the radiation emitted after linearly polarized stimulation is qualitatively similar to that after circularly polarized stimulation.

As previously discussed,the electric field measured via electro-optic sampling is generated by a time-varying current in the sample. The temporal profile photocurrent responsible for the electric field can thus be estimated using the indefinite integral $\vec{J}(t) = \int_0^t \vec{E}(t')dt'$. Fig 3.4c shows that the photocurrent thus calculated vanishes at long times, and hence the photoexcitation process does not generate a persistent current. Fig 3.4d shows the spectra of the circular dichroism in TaAs parallel to the crystalline non-polar axes, measured for both the $\langle 101 \rangle$ and $\langle 112 \rangle$ faces. The emission spectrum from the ZnTe calibration sample is re-scaled and plotted for comparison. The striking similarity between the spectra of ZnTe

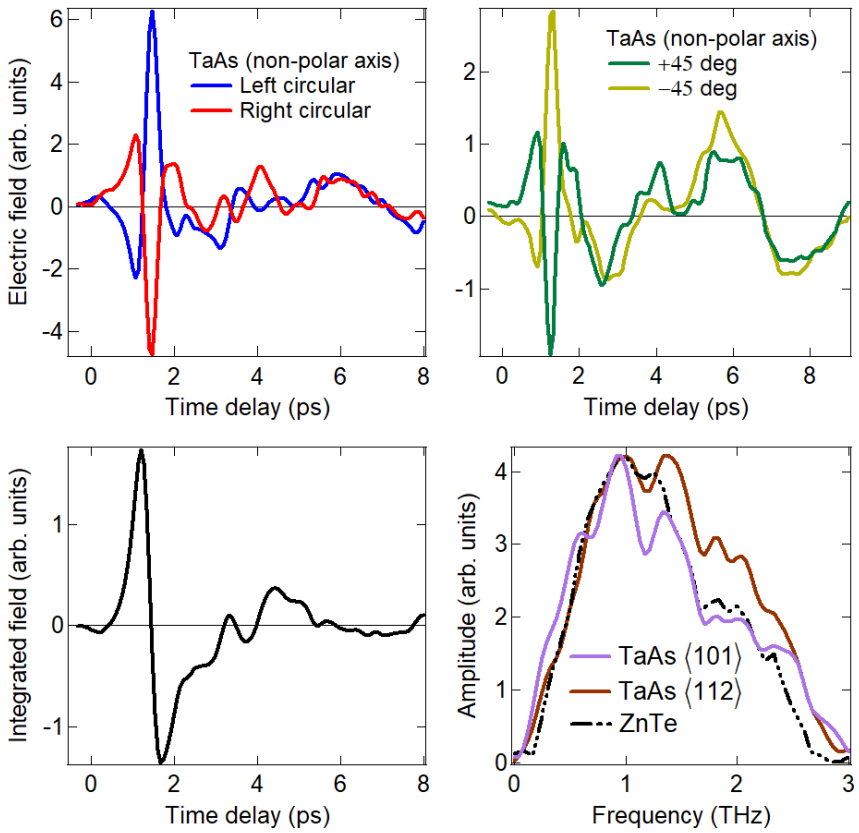

Figure 3.4: Terahertz radiation emitted with polarization along the sample $\hat{y}$-axis by laser pulses incident on the $\langle 101 \rangle$ face in (a) left- and right-circularly polarized states, and (b) linearly polarized states at $\pm 45^{\circ}$ to the polar direction, as a function of time delay between stimulation and measurement. The radiated electric field is seen to depend strongly on the polarization state of the stimulating laser pulses. The indefinite time integral (c) of the difference between the electric field stimulated by left and right circularly polarized laser shows that there is no net current given by $\vec{J} = \int \vec{E} dt$. The signal has sharp variations in the time domain, a fact borne out in the Fourier transform (d) of the difference between the electric field stimulated by left and right circularly polarized laser radiation for both the $\langle 101 \rangle$ and $\langle 112 \rangle$ faces, respectively. The emission spectrum from the ZnTe calibration sample is re-scaled and plotted for comparison.

and circular dichroism in TaAs suggests that the underlying mechanism for both effects is similar, namely optical rectification (eq. 3.2).

3.4 PGE along polar direction

While an instantaneous circular dichroism effect is seen when electric field is measured parallel to the non-polar directions, we observe an effect with very different characteristics when the radiated electric field is measured along the polar directions. Fig 3.5a,b show the radiated electric field with polarization parallel to the respective in-plane polar directions, with light incident on faces $\langle 101 \rangle$, $\langle 112 \rangle$ respectively. The pulse shapes show a long lived signal with measurable amplitude up to 6 ps delay from the incidence. The corresponding spectra (Fig 3.5c) for the electric field in frequency domain have a significantly lower bandwidth, especially compared with (Fig 3.2b) and (Fig 3.4b), with spectral peaks below 0.5THz and almost no measurable signal over 1.5THz.

As described in § III, if the radiated field changes significantly over the timescale of the laser pulse, a significant fraction of the spectral weight would be carried in a broadband component that is limited in bandwidth only by the experimental apparatus. The spectra in Fig 3.4c show a vanishing spectral weight for the frequency range over 2THz, and hence we may conclude that the radiated electric field $\vec{E}_{\text{polar}}(t)$, and hence the induced photocurrent $\vec{J}_{\text{polar}}(t) = \int \vec{E}_{\text{polar}}(t')\, dt'$ are negligible for the duration of the pulse, that is $\vec{J}(t) \approx 0$ for $t < \tau_{\text{pulse}} = 100\text{fs}$. Thus, the photogalvanic effect along the polar direction builds up slowly over a time scale greater than that of the incident laser pulse.

Fig 3.5d shows the peak value of the radiated electric field as a function of the angle of the linearly polarized stimulating laser polarization. While the electric field along the non-polar direction oscillates between positive and negative values characteristic of a signal generated by optical rectification, the electric field parallel to the polar direction is virtually independent of the direction of linear polarization of the incident laser. In addition to the peak value, the pulse shape of the electric field pulse radiated along the polar axis is constant for linearly polarized stimulating laser at various angles of polarization (Fig 3.5b), as well as to whether the incident laser is linearly or circularly polarized.

Figure 3.6b shows that the observed photogalvanic effect is virtually independent of sample temperature, which is consistent with the underlying mechanism relying only on the instantaneous temperature of the excited electron gas.

3.5 Anisotropic relaxation of hot carriers

The long lived structure in the electric field radiated parallel to polar direction, as well as the almost independence of the signal on the incident laser polarization, cannot originate from instantaneous physical processes such as shift current and non-resonant optical rectification. However, it is possible to generate photocurrents in a material through incoherent or stochas-

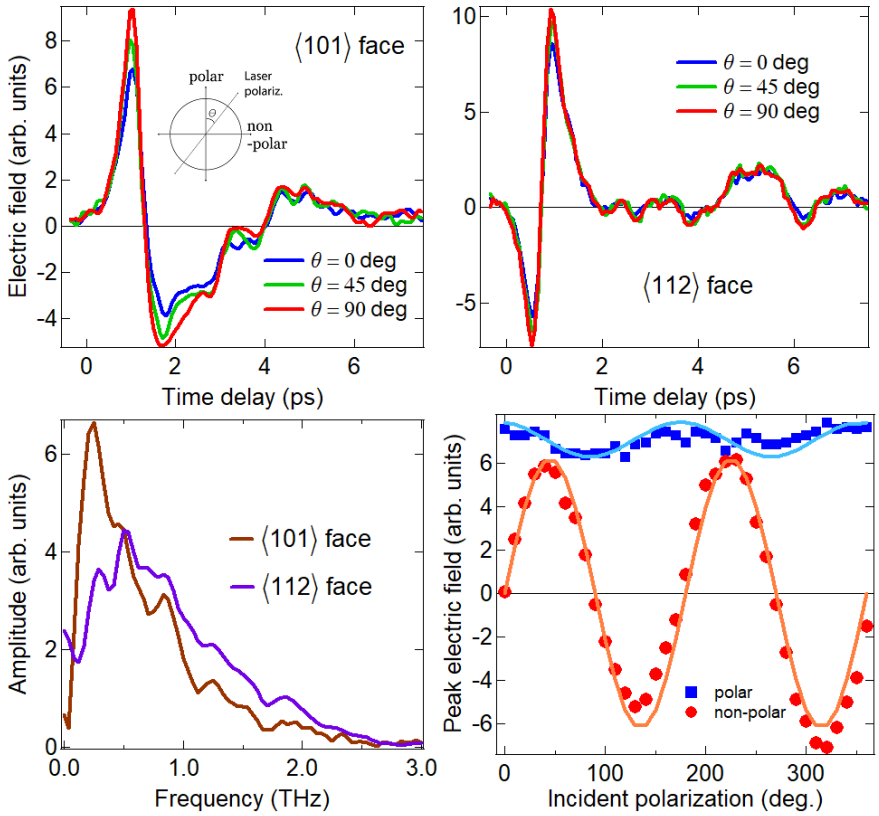

Figure 3.5: Terahertz radiation emitted with polarization along the in-plane polar axis by laser pulses incident on (a) the $\langle 101 \rangle$ face and (b) $\langle 112 \rangle$ face, the in various linearly polarized states. (c) Fourier transform of the emitted electric field from the $\langle 101 \rangle$ face with polarization parallel to $(1, 0, -1)$ (d) Radiated electric field from the $\langle 101 \rangle$ face measured at it's peak value in the time trace, as a function of the angle between the polarization of the linearly polarized stimulating radiation, and the $(0, 1, 0)$ axis. The radiated electric field along the $(1, 0, -1)$ has a significantly weaker dependence on the stimulating light polarization when compared with the electric field radiated along the $(0, 1, 0)$ direction.

tic processes [24]. In thermodynamics and statistical physics, a Brownian ratchet is a heat engine that uses mechanical asymmetry to transfer energy from a hot bath to a cold bath while performing work. The working of a Brownian ratchet is a fundamental consequence of the Second Law of Thermodynamics and is essential to understanding applications such as molecular motors [12, 17]. Analogously, in the case of photoexcited materials, a "hot gas" of photoexcited electrons surrounded by a cold lattice may drive a current due to anisotropic scattering. This effect is known as the Ratchet photogalvanic effect, and has been observed in materials with artificially induced asymmtery [19, 34]. These incoherent scattering processes include electron-phonon scattering, electron-electron scattering, and impurity scattering. Incoherent scattering processes are generally described with the momentum-space scattering

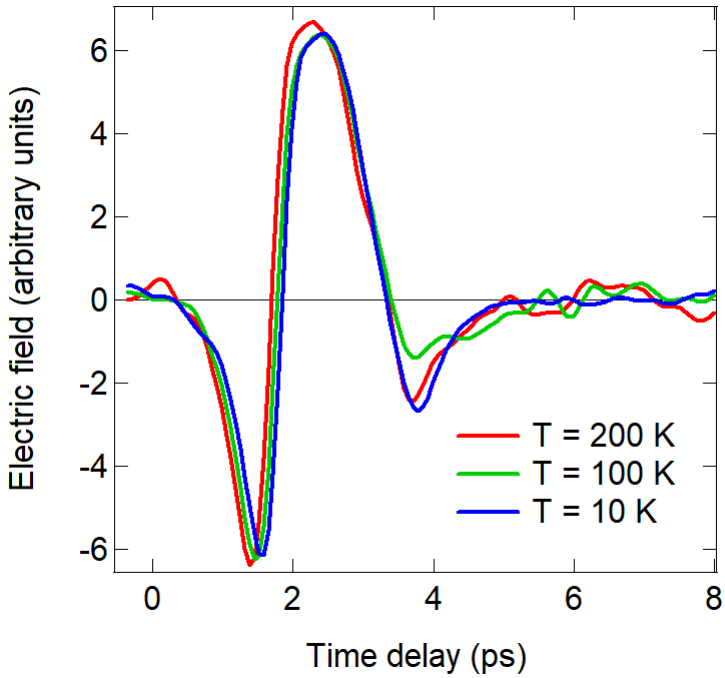

Figure 3.6: Terahertz electric pulse emitted along the sample $(1, 0, -1)$ direction at various sample temperatures. The photogalvanic effect is observed to be essentially independent of temperature

coefficient $W_{kk'}$ which is a scattering rate from a Bloch state of the momentum k to that of k'. Interestingly, in inversion broken systems, the scattering coefficient $W_{kk'}$ breaks the detailed balance (defined by $W_{kk'} = W_{k'k}$) due to asymmetric scattering (i.e., $W_{kk'} \neq W_{k'k}$). Asymmetric scattering induces transient asymmetric electron distribution in the momentum space, and hence, transient current in the process of relaxation into the high-temperature thermal state. Broken detailed balance in inversion broken systems can be induced by, for example, asymmetry in matrix elements of electron-phonon scattering, nonzero Berry curvature of Bloch electrons, and polar structure of impurity potential.

To substantiate this idea, we show typical time evolution of nonequilibrium distribution $f_k(t)$ and transient current $J(t)$, by using the simplest model of asymmetric scattering rate $W_{kk'}$ which is obtained from triangle impurity potential as shown in figure 3.7(a). The time evolution $f_k(t)$ is obtained by solving the Boltzmann equation [4, 3],

$$\frac{df_k(t)}{dt} = \int dk'(W_{kk'}f_{k'} - W_{k'k}f_k). \tag{3.3}$$

Here the first and second terms describe the electrons scattered into the state k and those scattered out of the state k, respectively. For simplicity, we suppose that photoexcited

carriers undergo incoherent scattering within a high-energy band that has isotropic band structure in the $k_x - k_z$ plane. Specifically, the scattering takes place within the circle defined by $|\mathbf{k}| = k_F$ in which Bloch states share the same energy. The scattering rate is obtained from the impurity in figure 3.7(a) which is assumed to be an isosceles right triangle with the length of the base $2b$ and the density n. Electrons hitting the triangle impurity are specularly reflected with respect to the side of the triangle. In this case, the scattering rate $W_{kk'}$ is deduced from the cross section of the impurity for the scattering process $k \to k'$. The scattering rate is the order of $bv_F n$ with the group velocity v_F at $|\mathbf{k}| = k_F$, which results in the typical relaxation time $\tau = 1/bv_F n$.

The transient current is obtained from the nonequilibrium distribution function as

$$J(t) = \int dk \; v_k \; f_k(t), \tag{3.4}$$

with the group velocity v_k. Since $W_{kk'}$ has an asymmetric part due to broken detailed balance, the matrix $W_{kk'}$ can generally have complex eigenvalues. The imaginary parts of the eigenvalues result in damped oscillation in $f_k(t)$ and $J(t)$. Now, in order to apply this procedure to TaAs, we need to determine the initial nonequilibrium distribution $f_k(t = 0)$ right after the pulse irradiation. Here we assume that the pump pulse excites electrons at Weyl nodes into a high energy trivial band having isotropic parabolic dispersion in the $x - z$ plane. In this case, the initial electron distribution in the parabolic band should look like the one in figure 3.7(b). In particular, this initial distribution does not depend on the polarization of the pump light because the rate of the photoexcitation into a trivial band is mostly determined by light intensity only. The time evolution of $f_k(t)$ in figure 3.7(c) shows that broken detailed balance induces asymmetric intermediate distribution along the k_z direction even though the initial distribution is symmetric along the k_z direction. In the later time, $f_k(t)$ relaxes into the isotropic thermal distribution as shown in figure 3.7(d). Accordingly, there appears nonzero transient current $J_z(t)$ along the z direction (Figure 3.7(e)), as a consequence of asymmetric intermediate distribution along k_z. The radiated electric field is proportional to the time derivative of the current dJ_z/dt which is shown in figure 3.7(f) and well reproduces the oscillatory behavior in the measured THz electric field (Figure 3.5). Thus we conclude that the long lived THz signal in the $(x - z)$ direction after the pulse light irradiation arises from the dynamics of photoexcited carriers induced by incoherent scattering that breaks the detailed balance.

In conclusion, we measured the photogalvanic effect in the Weyl semimetal TaAs. Along the non-polar direction in TaAs, the induced current consists entirely of circular dichroism that changes sign depending on the sense of the circular polarization of the stimulating radiation. Along the non-polar direction, we observe a photogalvanic effect that is consistent with a thermodynamic scattering driven photocurrent that is caused by anisotropic scattering of charge carrier under the condition of broken detailed balance. Thermodynamic scattering processes provide an interesting venue to study the low energy dynamics of charge carriers in

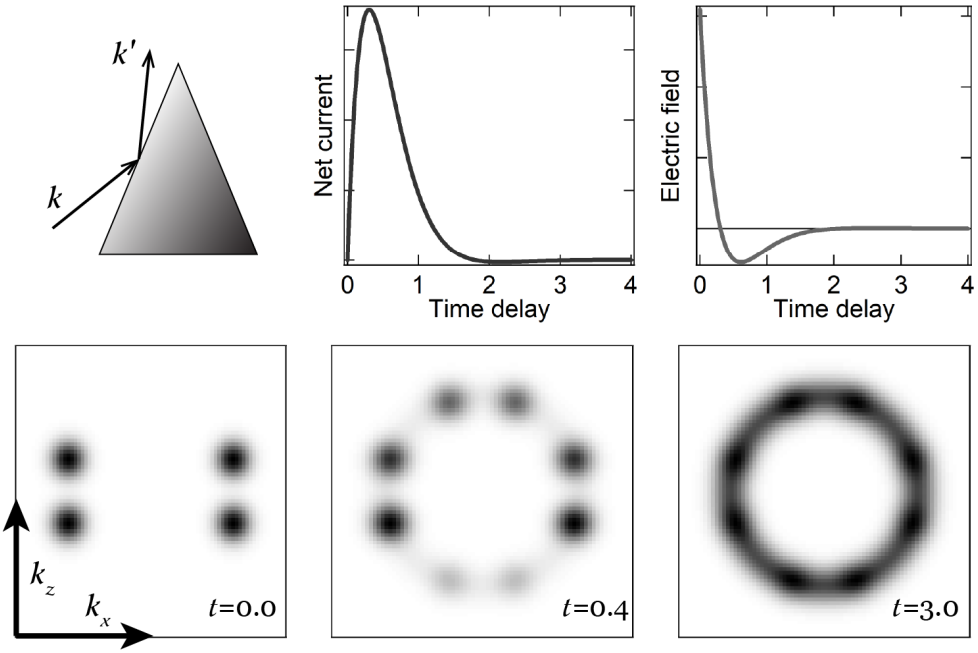

Figure 3.7: Transient current response induced by broken inversion symmetry. (a) Asymmetric scattering by triangle impurity potential. (b) Transient current $J_z(t)$ along the z direction, in units of ev_F/a. (c) Time derivative of current $dJ_z(t)/dt$ which is proportional to radiated electric field, in units of $ev_F/a\tau$. (d-f) Nonequilibrium distribution function $f_k(t)$ at (d) $t = 0$, (e) $t = 0.4$, and (f) $t = 3$. Here τ, v_F and a are typical relaxation time, the group velocity, and the lattice constant. Figure courtesy of T. Morimoto, provided through private communication.

Weyl semimetals, and point towards potential applications of these materials as broadband detectors of light in the far infrared regime.

Chapter 4

Resonant nonlinear optical conductivity

As mentioned in Chapter 2, while we established the existence of giant anisotropic nonlinear optical susceptibility in the transition metal monopnictides, the relationship between the nonlinear optical responses and the underlying microscopic physics remained an open problem. An approach to addressing this question empirically is by studying the second harmonic generation response of TaAs as a function of the incident laser wavelength. By studying this spectrum, we can hope to understand the relevance of the wavefunctions and the energy level distributions in the band structure of TaAs, especially as the incident photon energy is lowered from the visible range to the near, and mid-infrared range.

4.1 Wavelength dependent second harmonic spectroscopy

Two of the key challenges in studying the spectrum of second harmonic generation in materials are the abilities to generate and to detect pulsed laser beams of visible and infrared light. We have already described the value added by using laser sources with ultrashort pulses in studying nonlinear optical properties. For generating femtosecond pulses of laser with wavelengths from 800 nm to 2500 nm, we used a Coherent® Astrella™ integrated Ti:Sapphire amplifier that generates 50fs pulses of light at wavelength 800nm and a repetition rate of 5 kHz. The laser beam from the Astrella is then sent to a Light Conversion® TOPAS Twins™ optical parametric amplifier, that can output laser pulses of pulsewidth < 100 nm, with wavelengths from 800 nm to 2600 nm.

For detecting the radiated second harmonic light, recall that the intensity of second harmonic generated light from materials in reflection geometry is too low to be detected by conventional photodetectors. A multialkali PMT such as the one used in the single-wavelength SHG measurement can be used to detect SHG generated by incident light in the

near-infrared region of the spectrum. The Hamamatsu® R12829 PMT that was used here has a upper detection wavelength cutoff of 800nm. Thus, the PMT is able to detect SHG radiation stimulated by incident photon wavelengths of up to 1600 nm. For wavelengths higher than 1600 nm, we used conventional semiconductor based photodiodes for detection, however, we coupled the photodiodes to a Cremat® 110 charge amplifier module to significantly enhance the signal-to-noise ratio, and hence to enable detection of very low intensity light. We used a Si-photodiode (sensitivity up to 1000nm) to detect SHG stimulated by incident wavelengths from 1500nm to 1900nm, and an InGaAs-photodiode (sensitivity from 800nm to 1250nm) to detect SHG stimulated by incident wavelengths from 1700nm to 2400nm.

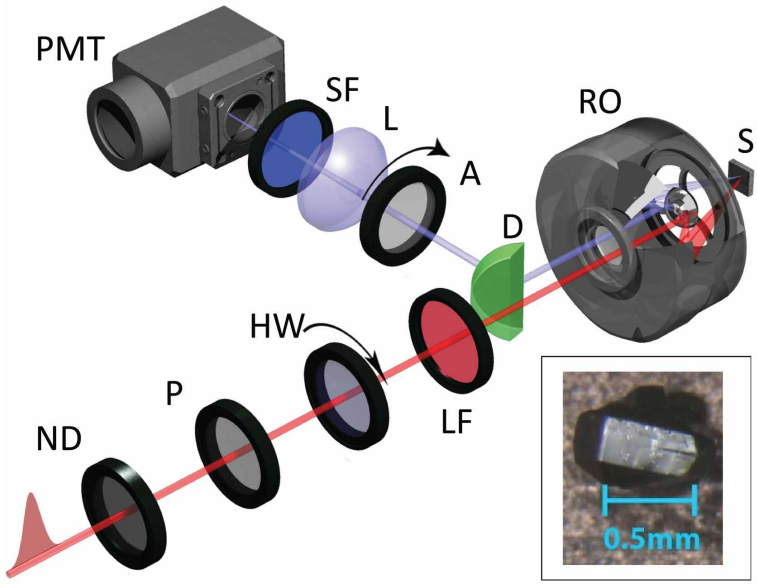

Figure 4.1: Modified apparatus used to study SHG response of TaAs at various incident wavelengths. Optical components including the ND filter (ND), Polarizer (P), Halwave plate (HW), D-cut mirror (D), analyzer (A), Lens (L) were chosen to be broadband capable, that is to be usable for all wavelengths between 800nm and 2500nm. The longpass (LF) and shortpass (SF) filters were altered along with the incident wavelength as necessary. Another key difference with the apparatus used to study single-wavelength SHG was the use of a reflective objective (RO) to focus the incident beam, and re-collimate the generated SHG beam. This is to avoid wavelength dependent focal length and other artifacts of conventional microscope objectives. Figure courtesy of D. Torchinsky, obtained through private communication.

Figure 4.1 shows a schematic of the experimental apparatus used to measure the SHG response from TaAs. While the components used are similar to those shown in figure 2.2, the primary difference was that the components used here (including the ND filters, polarizers, waveplates, and lenses) were broadband compatible. A reflective objective was used to avoid

wavelength dependent properties of conventional microscope objectives, such as wavelength dependent absorption and refractive index. In addition, sets of long pass and shortpass filter stacks were used to clean the incident and the radiated light wavelengths, respectively. These stacks were replaced with every change of the incident wavelength.

4.2 Polar patterns and tensor components

As described in section 2.2, the intensity of the second harmonic generation radiation was measured in polarization channels: *parallel*, *vertical*, and *horizontal*. Figure 4.2 shows the SHG intensity as a function of incident polarization angle for various incident laser wavelengths.

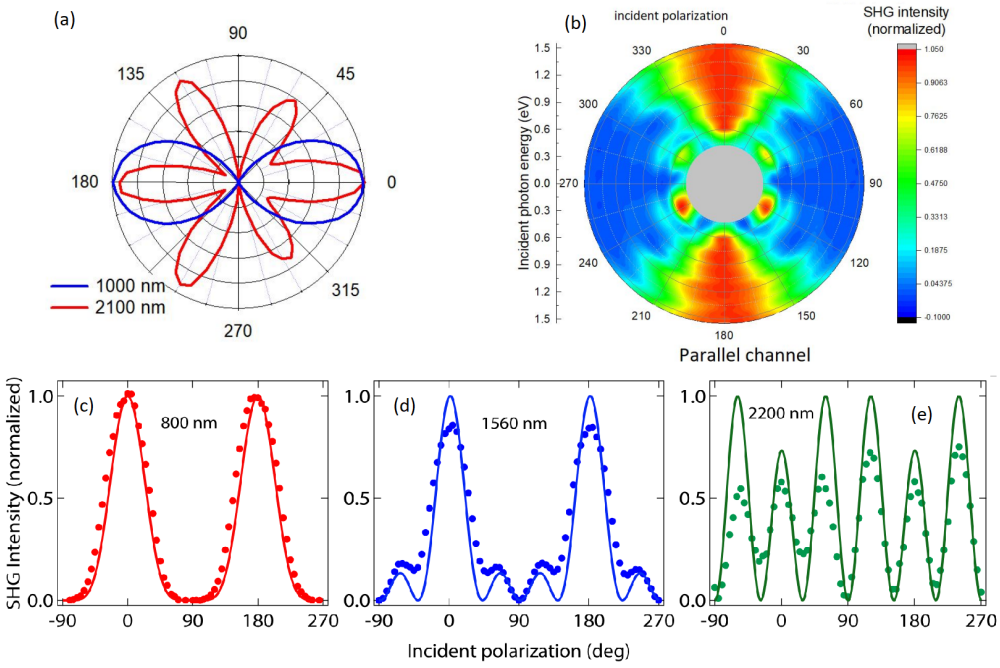

Figure 4.2: SHG intensity as a function of incident polarization angle for various incident laser wavelengths. (a) Contrast between the polar pattern at near-infrared wavelength (1100nm) and mid-infrared wavelength (2500nm). (b) A polar color plot showing the evolution of the polar pattern as a function of incident photon energy from 1.55 eV (800nm) to 0.5 eV (2500 nm). (c-e) SHG intensity in the parallel channel along with best fits for three representative wavelengths, 800nm, 1560nm, and 2200nm.

As in chapter 2, to extract the relative amplitudes of the tensor components, we fit the intensity from the *parallel*, *vertical*, and *horizontal* channels for each wavelength with equations 2.4, 2.6, and 2.7 respectively, to extract the values of χ_{eff}, χ_{zxx}, and χ_{xzx} as

functions of wavelength. Appendix C describes a series of correction factors that account for a number of wavelength dependent artifacts, such as the diffraction limited spot size, the transmission coefficients of the various filters, the intensity of the laser output from the OPA, and so on. For the absolute quantitative values of the nonlinear susceptibility, we used the previously published values at 800nm as anchor points.

4.3 Spectrum of SHG in TaAs

From the perspective of theoretical analysis, the nonlinear optical conductivity $\sigma^{\text{shg}}_{ijk}(\omega)$ is more convenient to deal with than the susceptibility χ. The two are related by the equation[1]:

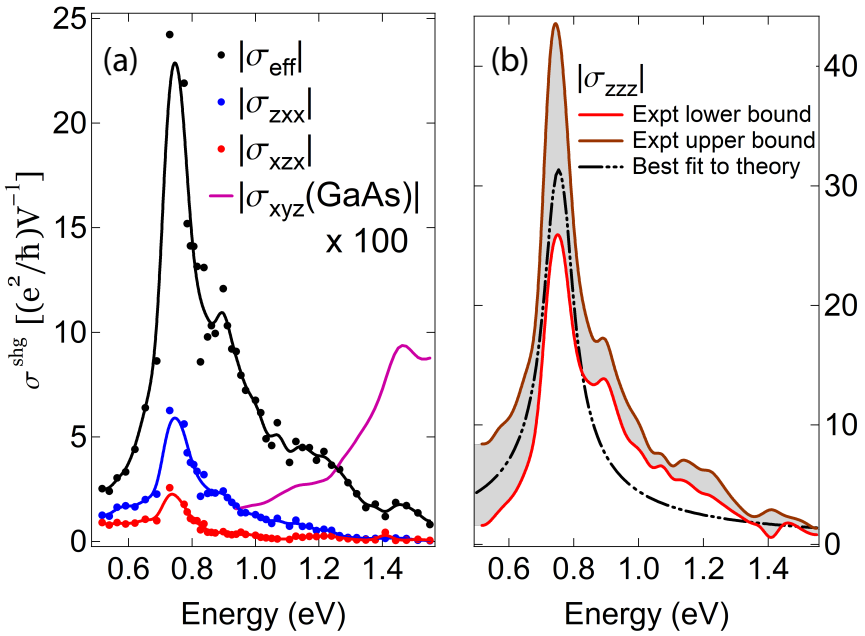

Figure 4.3: (a) Spectrum of components of the nonlinear optical conductivity of TaAs over the observed incident photon energy range from 0.5eV to 1.55 eV. The nonlinear optical conductivty of GaAs over the same range is multiplied by 100 and plotted for comparison. (b) Upper and lower bounds for the χ_{zzz} component of the conductivity, estimated from the components χ_{eff}, χ_{zxx}, χ_{xzx} that are obtained by direct fits to the data.

$$\sigma^{\text{shg}}_{ijk}(\omega) = i\epsilon_0\ \omega\ \chi^{\text{shg}}_{ijk}(\omega) \tag{4.1}$$

[1] $\sigma^{\text{shg}}_{ijk}(\omega)$ is an abbreviated way to refer to the nonlinear optical conductivity in the context of second harmonic generation, also denoted as $\sigma^{(2)}_{ijk}(\omega, \omega; 2\omega)$

Figure 4.3a shows the spectra for the components of σ^{shg} thus calculated for all incident photon energies. While it is not possible to extract the value of σ_{zzz} by direct fits to the data, we are able to put upper and lower bounds to its value using the relations (figure 4.3b):

$$\left|\sigma^{\text{high}}_{\text{zzz}}(\omega)\right| = |\sigma_{\text{eff}}(\omega)| + |\sigma_{\text{zxx}}(\omega)| + |\sigma_{\text{xzx}}(\omega)|$$
$$\left|\sigma^{\text{low}}_{\text{zzz}}(\omega)\right| = |\sigma_{\text{eff}}(\omega)| + |\sigma_{\text{zxx}}(\omega)| - |\sigma_{\text{xzx}}(\omega)|$$

We see the nonlinear optical response of TaAs at 1.55 eV that has already been measured to be an order of magnitude larger than any other known material, is merely the tail of a large peak in the second harmonic response of TaAs that is centered at 0.7 eV. At it's peak, TaAs has a nonlinear optical conductivity that is nearly three orders of magnitude larger than GaAs at the same incident photon energy. Furthermore, the anisotropy in the relative amplitudes of the tensor components $\sigma^{\text{high}}_{\text{zzz}}(\omega)$ and $\sigma^{\text{high}}_{\text{zxx}}(\omega)$, and $\sigma^{\text{high}}_{\text{xzx}}(\omega)$ observed at 1.55 eV is also present at lower incident photon energies.

4.4 The Rice-Mele model

The strong anisotropy and the sharp resonance at 0.7 eV motivate a minimal theoretical model as a 1-D tight binding Hamiltonian. The Rice-Mele (R-M) model is a model to describe low-lying excitations in a linearly conjugated diatomic polymer [38], and has recently been used in calculations of shift current and electric polarization in inversion symmetry breaking mono-layer chalcogenides [36]. We thus use a simplified model for the TaAs crystal as an array of 1-D R-M chains with inter and intra-chain interactions as tuning parameters (see figure 4.4). The two-level R-M Hamiltonian with inversion broken along the z-direction can be written as

$$H_{RM} = t\cos\left(\frac{k_z a}{2}\right)\sigma_x + \delta\sin\left(\frac{k_z a}{2}\right)\sigma_y + \Delta\ \sigma_z \tag{4.2}$$

where σ_i are the Pauli matrices. The inversion symmetry in the diatomic chain is broken by the on-site energies $\pm\Delta$, and by the hopping potentials $t \pm \delta$. As shown in figure 4.4, the aforementioned array of 1-D chains better approximates the 3-D TaAs crystal, by adding an interchain hopping term $t_{AB}(\cos k_x a_x + \cos k_y a_y)$ to the coefficient of σ_z in H_{RM}, where $t_{AB} \equiv t_{\|A} - t_{\|B}$. Following the calculation in ref. [41] (see supplemental information in [35]), we can calculate the photoinduced shift current in this model

$$\sigma^{\text{shift}}_{\text{zzz}}(\omega) = \frac{2e^3}{\hbar\Delta}\left(\frac{1}{4\pi}\right)^3 \frac{c^2}{ab} F\left(\tilde{\omega}; \tilde{\delta}, \tilde{t}, \tilde{t}_{AB}\right) \tag{4.3}$$

where F is a dimensionless function of the frequency ω (the tildes indicate normalization by Δ); and a, b, c are lattice constants in the x, y, z directions respectively. We can calculate the real part of the SHG nonlinear optical conductivity by using the relation [31]:

$$\text{Re}\{\sigma^{\text{shg}}_{\text{zzz}}(\omega)\} = -\frac{1}{2}\sigma^{\text{shift}}_{\text{zzz}}(\omega) + \sigma^{\text{shift}}_{\text{zzz}}(2\omega) \tag{4.4}$$

That is, the SHG conductivity response is the sum of the response conditions where the

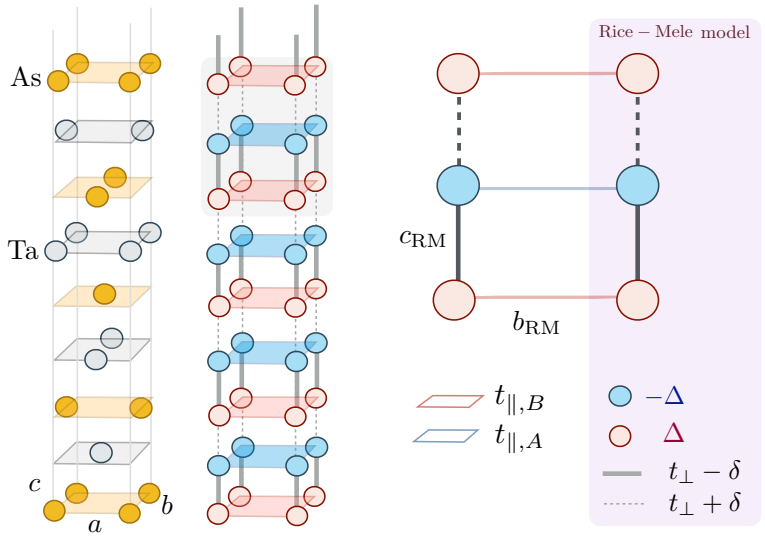

Figure 4.4: The Rice-Mele model for nonlinear optical response in a material. (Left panel) An array of Rice-Mele chains is used as a simplified model of the TaAs crystal structure for calculating SHG response. (Right panel) The various parameters used that account for the inversion symmetry breaking in the Rice Mele model. Figure courtesy of A. G. Grushin, obtained through private communication.

shift frequency is resonant with the direct energy gap (the "one photon" term) and where the shift frequency is resonant with one-half the direct energy gap (the "two photon" term). The dashed curve in figure 4.3b is the best fit to the experimentally obtained limits on $\sigma^{\mathrm{shg}}_{zzz}$ with the 2-photon term in equation 4.4 using the fit parameters $\tilde{t} = 1.5$, $\tilde{\delta} = 1.4$, $\tilde{t}_{AB} = 0.02$, $\tilde{\Delta} = 0.428$. The lattice parameters for TaAs are $c = 1.165$nm, $a = b = 0.344$nm [32].

4.5 Sum rule for nonlinear optical conductivity

The nonlinear optical conductivity for the Rice-Mele model, as calculated in equation 4.3 has a curious property, namely, if we define $\Sigma^{\mathrm{shift}}_{zzz}$ to be the integral of $\sigma^{\mathrm{shift}}_{zzz}$ over all frequencies, we find:

$$\Sigma^{\mathrm{shift}}_{zzz} \equiv \int \sigma^{\mathrm{shift}}_{zzz}(\omega) d\omega \ = \frac{e^3}{\hbar^3}\frac{c^2}{ab} G(\tilde{t}, \tilde{\delta}) \tag{4.5}$$

where G is also a dimensionless function of the dimensionless parameters that evaluates to:

$$G(\tilde{t}, \tilde{\delta}) = \tilde{t}\tilde{\delta}\frac{E_2(\frac{\tilde{\delta}^2 - \tilde{t}^2}{1+\tilde{\delta}^2})}{(1+\tilde{t}^2)\sqrt{1+\tilde{\delta}^2}} \tag{4.6}$$

E_2 being the complete elliptic integral of the second kind. The function $G(\tilde{t}, \tilde{\delta})$ reaches

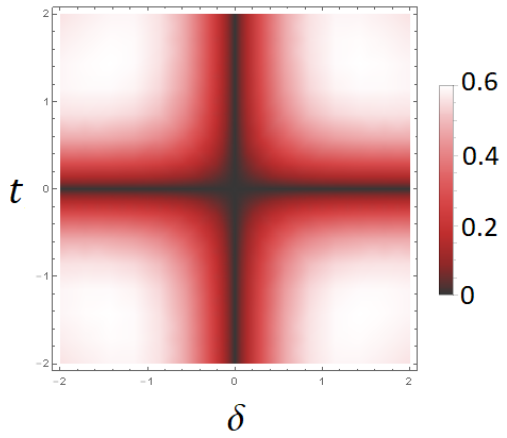

Figure 4.5: $G(\tilde{t}, \tilde{\delta})$ over the parameter space of $\tilde{t}$ and $\tilde{\delta}$. The global maximum of G is 0.604, however, G reaches a value within 10% of its maximum for a large part of the $\tilde{t} - \tilde{\delta}$ phase space. A nonlinear optical conductivity approaching the upper bound is thus not an especially uncommon circumstance.

a global maximum of $\pi 3^{-3/2} \approx 0.604$ at $\tilde{t} = \tilde{\delta} = \sqrt{2}$. As figure 4.5 shows however, the value of $G(\tilde{t}, \tilde{\delta})$ is close to its maximum over a large fraction of the $\tilde{t} - \tilde{\delta}$ phase space. The implication here is that there exists a fundamental upper bound on the frequency integral of the nonlinear conductivity in the R-M model. To thus maximize the nonlinear optical response in a material that is proximately R-M, a leading strategy would be to synthesize the largest possible value for the crystal geometry coefficient $\frac{c^2}{ab}$, which is achieved in crystals with higher anisotropy.

4.6 Guage invariant cumulants

The fact that the frequency integral of the nonlinear optical conductivity in the R-M model is bounded by fundamental constants and geometric factors is not merely a coincidence, but is a consequence of a theorem relating optical properties of matter with the geometrical parameters of Bloch wavefunctions known as "guage-invariant cumulants" (GICs) [35]. In statistics and probability theory, cumulants of a probability distribution X are defined as

$$C_1 \equiv \langle X^i \rangle \tag{4.7}$$

$$C_2 \equiv \langle X^i X^j \rangle - \langle X^i \rangle \langle X^j \rangle \tag{4.8}$$

$$C_3 \equiv \langle X^i X^j X^k \rangle + 2 \langle X^i \rangle \langle X^j \rangle \langle X^k \rangle - \langle X^i X^j \rangle \langle X^k \rangle - \langle X^i \rangle \langle X^j X^k \rangle - \langle X^i X^k \rangle \langle X^j \rangle \tag{4.9}$$

and so on, where $\{i, j, k\} \in \{x, y, z\}$ are spatial indices. The cumulants measure the respective levels of "skewness" of the distribution, as illustrated in figure 4.6. The gauge invariant

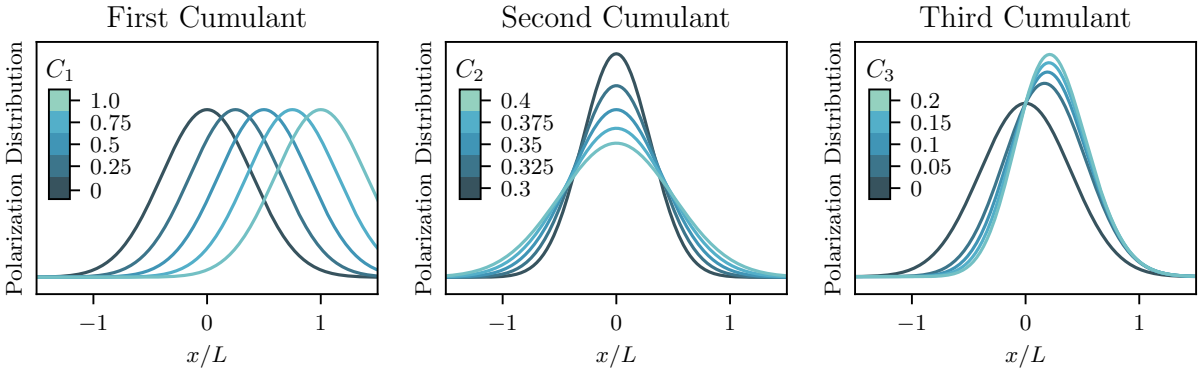

Figure 4.6: Schematic representation of polarization distribution corresponding to Bloch wavefunctions with various values of the three GICs C_1, C_2, and C_3. Figure courtesy of D. Parker, obtained through private communication.

cumulants C_i are both a measure of the assymetry of the electron wavefunction distribution within the unit cell, and also of the electromagnetic response of the material to incident radiation. The first cumulant is related to the Berry connection $\mathbf{A}_n(\mathbf{k})$ of the wavefunction, and hence the net electric polarization $\langle \mathbf{P} \rangle$.

$$\langle \mathbf{P} \rangle = \frac{e}{V} C_1 = e \sum_{n \text{ occ}} \int d\mathbf{k} \mathbf{A}_n(\mathbf{k}) \tag{4.10}$$

Similarly, the second cumulant is related to the linear optical response of the system, which using the fluctuation-dissipation theorem can be expressed as:

$$\frac{\pi e^2}{V^2 \hbar} C_2^{\alpha\beta} = \int \frac{d\omega}{\omega} \text{Re}\{\sigma^{\alpha\beta}(\omega)\} \tag{4.11}$$

As is demonstrated in reference [35], the nonlinear optical conductivity can be related to the third cumulant C_3 using the relation

$$\Sigma_a^{\text{shift}} \equiv \int \sigma_{\text{aaa}}^{\text{shift}}(\omega) d\omega = \frac{2\pi e^3}{V \hbar^2} C_3^a \tag{4.12}$$

Chapter 5

Giant $\chi^{(2)}$ materials in applications

Materials with $\chi^{(2)}$ susceptibility are widely used in commercial applications for frequency doubling and optical parametric oscillators [14]. Current applications primarily rely on insulating oxide compounds such as $LiNbO_3$/PPLN, and KTP, which have relatively low nonlinear optical susceptibility, are able to compensate by virtue of being transparent at laser wavelengths and allowing buildup of nonlinearity through phase matching. As we have shown, the TMMP family of Weyl semimetals have nonlinear optical susceptibilities that are two to three orders of magnitude larger than these conventional materials, and hence should be useful in nonlinear optics applications. This chapter proposes nonlinear optics aplications of the TMMP materials that play on their material properties.

5.1 Near field second harmonic generation

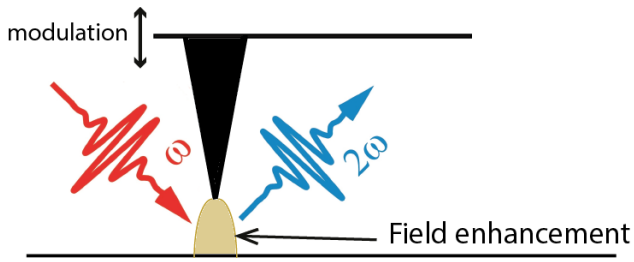

Figure 5.1: Schematic of apparatus to study near field second harmonic generation below the wavelength dependent diffraction limit.

A preliminary challenge to these applications is presented by the fact that the TMMPs, in contrast with the insulating oxides, are metallic, and hence absorptive all the way down to zero frequency. Thus, the TMMPs have very large complex refractive indices that significantly lower the effective reflection geometry $\chi^{(2)}$ per the Bloembergen-Pershan correction parameter (equation 2.12). In addition, the TMMP materials are opaque at visible and IR

wavelengths with penetration depths < 200 nm, preventing the use of phase-matching techniques that allow high-efficiency frequency doubling in transparent nonlinear materials like the insulating oxides. Here I propose nonlinear optics applications of the TMMP materials on the nanometer scale, where their inherent advantages in large $\chi^{(2)}$ become more relevant.

Recent advances in near-field microscopy have made it possible to study optical phenomena with finer resolution than is allowed by the wavelength-dependent optical diffraction limit. One of the techniques for near field studies relies on using an AFM tip with sub-nanometer resolution to act as a dipole antenna to enhance the electric field of the incident light in the vicinity of the sample being studied. The same principle can be applied can be applied to studying second harmonic generation in the near field, where sensitive detection can be enabled by modulating the tip distance of the near field antenna at a set frequency that can be picked up using a lock-in detector (figure 5.1).

5.2 Pulse shaping below the diffraction limit

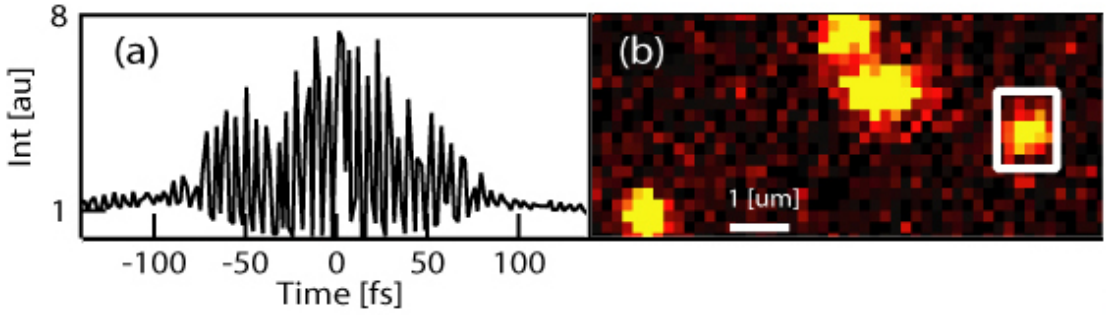

Figure 5.2: (a) Autocorrelation function of a 70fs laser pulse obtained through optical second harmonic generation in $Fe(IO_3)_3$ nanoparticles. (b) An optical SHG image of an ensemble of $Fe(IO_3)_3$ nanocrystals deposited on a microscope slide. The particle highlighted in the box was used for the autocorrelation data. Since TMMPs have a nonlinear susceptibility that is 2-3 orders of magnitude larger than that of $Fe(IO_3)_3$, a TMMP nano-FROG will greatly reduce acquisition time for pulse characteristics. Figures from Extermann et al., (2008) [10], reproduced with permission from the Optical Society of America.

Novel physical systems such as photosynthetic complexes and individual quantum dots are often studied using femtosecond pulsed lasers to better understand their electron dynamics. However, a key challenge in these studies is the lack of ability to characterize and control the ultrafast probes themselves, since dispersive optics such as lenses and objectives strongly affect the pulse width of laser pulses.

In traditional ultrafast optical laboratories, the dispersion and shape of femtosecond laser pulses is measured and controlled using techniques such as multiphoton intrapulse interference phase scans (MIIPS) and frequency-resolved optical gating (FROG). These techniques rely on using second harmonic generation in bulk nonlinear materials like -barium oxide (BBO) and $LiNbO_3$, where using crystals up to milimeters in thickness allows one to benefit from the higher efficiency generated by phase-matching in these crystals. However, milimeter sized crystals are impractical to use in a sub-diffraction limit nanoscale apparatus, hence motivating new ways of characterizing femtosecond laser pulses with sub-diffraction limit spatial resolution.

Recently, researchers have demonstrated success in using nanoparticles of nonlinear materials to address this concern, for instance with a nano-FROG using $Fe(IO_3)_3$ nanoparticles [10], and a nanoscale MIIPS based on $BaTiO_3$ and $Fe(IO_3)_3$ nanoparticles [1] (see figure 5.2). While these techniques are able to resolve laser pulse-widths of less than 70fs, they require several hours of data acquisition averaging given the small SHG signal. Thus since nano-FROG and nano-MIIPS are not limited by low penetration depths and TaAs and other TMMPs have nonlinear optical susceptibilities that are 360 times that of $Fe(IO_3)_3$ and 240 times that of $BaTiO_3$, we propose that using TMMP nanoparticles in these techniques has the potential to increase the signal strength by up to 4 orders of magnitude, and correspondingly reduce the acquisition time from several hours to mere seconds, making them practically viable as characterization tools.

Appendix A

Building a terahertz emission spectrometer

As described in Chapter 3, terahertz emission spectroscopy (TES) is a technique to study terahertz emission from a material when stimulated by incident visible or infrared laser radiation. Because the technique can be used to measure terahertz radiation in the ~ 1 meV energy range, it is also an effective, contactless probe of photogalvanic currents induced in a material by stimulating radiation. In this appendix, I describe the various essential components in setting up a terahertz emission spectroscopy apparatus.

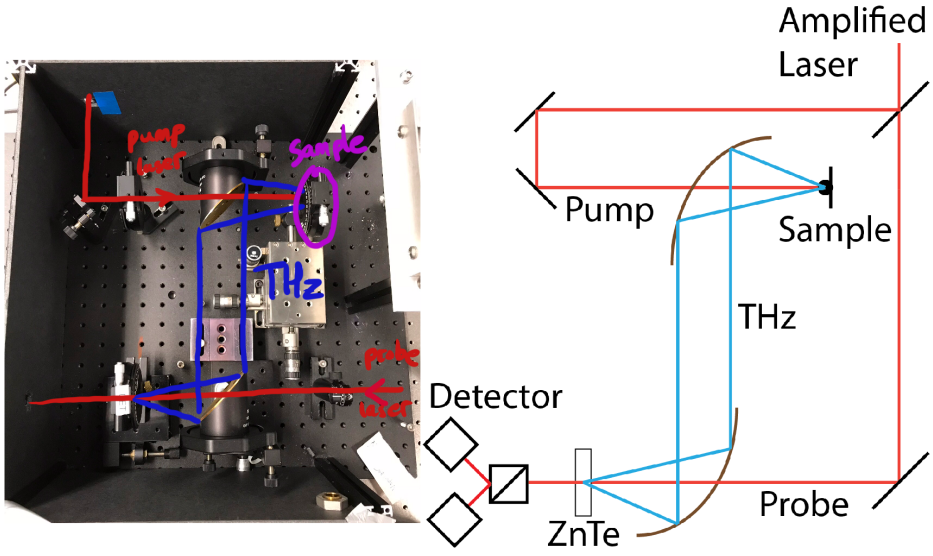

Figure A.1: (a) Photograph and (b) schematic of the apparatus for generating and detecting terahertz radiation in the terahertz emission spectroscopy (TES) experiment. Not shown: optical delay stage, and neutral density filters.

Amplified laser

The data presented in Chapter 3 was acquired with an apparatus based on the Coherent® RegA amplified laser that uses pulses from a Coherent® Mantis™ Ti:Sapphire oscillator. The Mantis provided 50fs pulses at a repetition rate of 80 MHz, and average power of ~ 250 mW. These were amplified by the RegA to have an average power of ~ 250 mW at a repetition rate of 250 kHz, which corresponds to a pulse energy of 3 μJ at 800 nm wavelength. Although other groups have reported success in measuring THz emission using laser pulses directly from an 80 MHz oscillator [39], we have so far not been able to replicate that.

More recently, we have successfully assembled a TES apparatus based on a laser with significantly lower repetition rate, and hence significantly higher pulse energy. Figure A.2 compares the THz pulse from a ZnTe sample as stimulated by the aforementioned 250 kHz pulsed laser, and by a 5 kHz pulsed laser with output pulses of ~ 1 mJ. Although one may expect a higher RMS noise level due to the lower repetition frequency of 5 kHz, this is more than outweighed by the gain in the electric field amplitude due to the higher pulse energy.

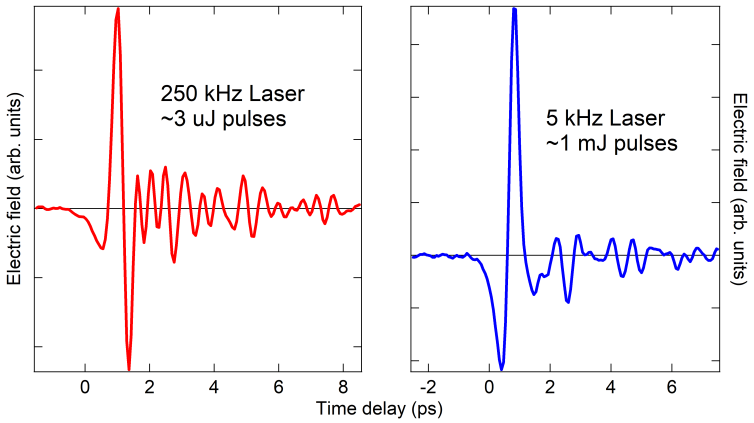

Figure A.2: Comparison of THz electric field generated by a ZnTe sample with substantially different pulse energies. Terahertz pulses generated by a (Left) laser operating at 250 kHz with a 3 μJ output (right) laser operating at 5 kHz with a 1 mJ output.

Optical components

Due to the substantial pulse energies involved, the various neutral density filters used to control the input intensity were "reflective" (as opposed to "absorptive") neutral density filters. The reflective filters have a thin metallic film of ITO that is more resistant to optical damage than the polymer materials typically used in absorptive filters.

The incident laser beams, in both the pump and probe segments, were focused on to the sample or the ZnTe detector respectively, using lenses. To avoid sample damage, and

also to avoid signal losses due to the diffraction limit of the terahertz electric field, we used lenses with significantly long focal lengths (100-200 mm), to focus the beams down to relatively large spot sizes of approximately 200-300 μm. In addition, a zero-order halfwave plate mounted on a motorized rotation stage was used in the pump beam to control the polarization state of the pump beam.

Optical path lengths

One of the key initial steps in aligning the TES apparatus is matching the delay lengths of the pump and the probe arms. That is, it is necessary to ensure that the path length from the **beamsplitter** to the **ZnTe detector** is equal. In the preliminary alignment stage, this can be done by using a simple tape measure to calculate distances between various optics, in order to get the pump and probe arm lengths equal to an accuracy of ± 1 cm. Note that this already accounts for a motorized optical delay stage on the pump arm. The motorized optical delay stage can then be stepped precisely in step sizes of 0.03 mm or smaller to precisely locate the overlap point of the pump and probe beams. The final positioning needs to be accurate to within 100 fs of time delay, that is, ~ 30 μm.

Sample geometry

Conventional experiments to study terahertz time-domain spectroscopy (THz-TDS) often rely on similar principles of laser stimulation to emit THz radiation that is then detected by electro-optic sampling. One of the differences that is essential to making TES a useful technique was prompted by the fact that several materials of interest for TES and photogalvanic studies (including the Weyl semimetal TMMPs) are metallic, and/or are not transparent to incident visible or infrared radiation. As shown in figure A.2, our initial measurements were performed with a ZnTe sample in the "reflection" geometry, that is, the THz radiation of interest is being emitted by the sample in the collinear but counter-propogating direction to the stimulating laser beam. In our measurements, the amplitude of the electric field in the "reflection" geometry was approximately one-half the amplitude in the more conventional "transmission" geometry.

Electro-optic sampling for THz detection

There are a number of noteworthy considerations when assembling an apparatus for electro-optic sampling (EOS). All the measurements described in Chapter 3 were performed with a ZnTe [110] crystal as the THz "detector" (see figure A.1 for detail). EOS works on the simple principle that in a nonlinear optical crystal, an applied electric field **E** (which is the terahertz radiation in our case) induces a change in the refractive index n_{ij} of the crystal by the relation

$$\Delta n_{ij} = r_{ijk} E_k \tag{A.1}$$

where r_{ijk} is the electro-optic sampling coefficient of the material. Since r_{ijk} and $\chi^{(2)}_{ijk}$ are tensors of the same rank in the same material, they are related to each other by a scalar number. Thus, we can use the SHG pattern of the same ZnTe crystal to determine the appropriate orientations when it is used for electro-optic sampling. The principle axes of the induced birefringence (that is, the eigenvectors of the Δn_{ij} matrix) are dependent on the polarization of the incident THz electric field. For the $[1, 1, 0]$ face of ZnTe, Δn_{ij} is maximized when $\mathbf{E}$ is parallel to the $(-1, 1, 0)$ axis (recall that ZnTe can only have one non-zero component of r_{ijk}, namely, r_{xyz}). Thus, as described in Chapter 3, we rotate the ZnTe crystal so that the $(-1, 1, 0)$ axis is parallel to the angle of polarization of $\mathbf{E}$ to be measured.

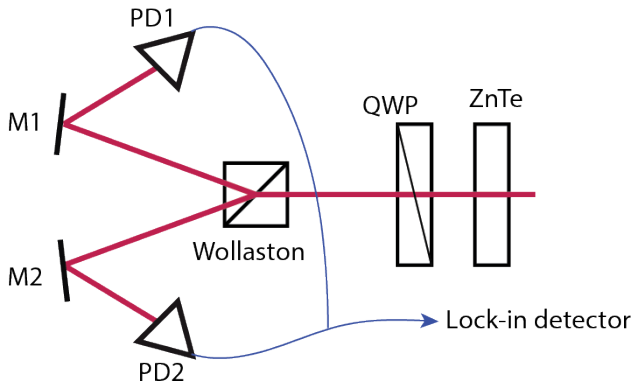

Figure A.3: Detailed schematic of electro-optic sampling used in the TES measurement apparatus. SHG polarimetry is used as a tool to find the ideal detection axes for ZnTe. A motorized rotation mount is used to precisely align the quarter-wave plate QWP, such that the intensities measured by the oppositely poled photodiodes PD1 (+) and PD2 (−) cancel each other.

The probe laser beam then passes through a quarter-wave plate (QWP), a Wollaston prism (to split the S, P polarization beams) that are then independently aligned into the oppositely poled photodiodes PD1, PD2 using mirror M1, M2 respectively. The photodiodes are chosen to have opposite poling, that is, PD1 is a cathode photodiode and PD1 is an anode photodiode, such that their readout measures only the difference in the light intensity from the S,P polarized beams. The QWP is mounted on a motorized rotation staged, and aligned precisely so that in the absence of $\mathbf{E}^{\mathrm{THz}}$, the balanced photodiodes have an output as close to zero as possible.

Appendix B

Quantitative evaluation of photogalvanic currents

The electro-optic sampling signal $S(t)$ (as measured by balanced detector $PD1 - PD2$), in a thin $\langle 110 \rangle$ ZnTe crystal, is related to the terahertz electric field by the relation [13] (see Appendix A):

$$S(t) = \int_{-\infty}^{\infty} \chi^{(2)}_{\text{eff; ZnTe}}(\omega_0, \Omega, \omega_0 - \Omega) E_{\text{THz}}(\Omega) e^{-i\Omega t} d\Omega \tag{B.1}$$

Given that for ZnTe, the measured peak signal ($\Delta I/I$) is 10^{-7}, and that $\chi^{(2)}_{\text{eff; ZnTe}} = 4.1\text{pm/V}$ [8] , we get peak electric field $E^{\text{peak}}_{\text{ZnTe}} \approx 20\text{kV/m}$. The Electric field (spectral density) radiated into free space by a time varying polarization (spectral density) $\vec{p}$ in a material of refractive index n is given by [9]

$$\vec{E}(\Omega, \vec{K}, z) \approx \frac{i\Omega}{2\epsilon_0 nc} t_n \vec{p}(\Omega, \vec{K}) \xi_{\text{pol}} \tag{B.2}$$

where Ω is the frequency of the radiated field, $\vec{K}$ is the transverse component of the wavevector, z is the distance from the interface, t_n is the Fresnel coefficient $t_n = \left(1 - \left|\frac{n-1}{n+1}\right|^2\right) \approx \frac{4}{n}$, $\vec{p}$ is the polarization spectral density, ξ_{pol} is the depth at which the source polarization is active. Using $n = 31$, $\xi_{\text{pol}} = 10\text{nm}$, $\frac{\Omega}{2\pi} = 1$ THz gives

$$\begin{aligned} \vec{p} &\approx \vec{E} \frac{\epsilon_0 n^2 c}{2i\Omega\xi_{\text{pol}}} \\ &\approx 0.4\text{C/m}^2 \end{aligned}$$

Shift current: The polarization density can be related to a possible shift current by [26]

$$\vec{J}_{\text{shift}} = \frac{eI_p}{\hbar\omega\xi_{\text{pol}}} \vec{r}_{\text{shift}} \tag{B.3}$$

where $\vec{J}_{\text{shift}} = \dfrac{\partial \vec{p}_{\text{shift}}}{\partial t}$

Assuming the entire polarization change occurs over the duration of the pulse, $\vec{J}_{\text{shift}} \approx \dfrac{\Delta \vec{p}_{\text{shift}}}{\Delta t} \approx 4 \times 10^{12} \text{A/m}^2$, and using *instantaneous* peak pump intensity $I_p = 30$ TW/m^2. Eq (3) then gives $\vec{r}_{\text{shift}} = 2\text{nm}$

Optical rectification: Assuming instantaneous peak pump intensity to be 30 TW/m^2, and ZnTe optical rectification constant $d_{14} = 69$ pm/V [47], optical rectification induced polarization 0.06 C/m^2

Appendix C

Data analysis for nonlinear spectroscopy

Wavelength dependent correction factors

Despite best efforts to maintain wavelength invariance, any experimental apparatus to study optical spectroscopy will have wavelength dependent features in various components that lead to artifacts in the data. These artifacts are especially large in a nonlinear spectroscopy experiment due to the stronger dependence on incident light, and hence need to be accounted for before the experimental data can be analyzed.

The initial values $\chi_{ijk,\text{fit}}$ were extracted by fitting the raw experimental polar data from the various "channels" using equations 2.4, 2.6, and 2.7. The final values $\chi_{ijk,\text{norm}}$ were used to calculate the σ_{ijk} components that are plotted in figure 4.3a. The following is a list of wavelength dependent artifacts that were identified, along with how they were calculated and accounted for.

1. FilterTransmission: transmission coefficient of bandpass filter (from Thorlabs). (see figure C.1b)
2. DetectorResponse: interpolated response functions for detectors
3. LaserPower: laser power after applying nominal ND filter values
4. LaserBand: measured laser bandwidth at various wavelengths, interpolated
5. $\text{FilterBandwidth} = \dfrac{.044 \times \lambda^2}{299.8 \times \text{LaserBand} \times 2.828}$, λ being the incident laser wavelength.
6. $\text{BP}_{\text{factor}}$: Bloembergen-Pershan factor (see equation 2.12, and figure C.1c)
7. An overall factor of λ to account for the fact that the diffraction limited spot size area, and hence the incident laser fluence on the sample scale quadratically with λ.

Give final calculated value:

$$\chi_{ijk,\mathrm{norm}} = \chi_{ijk,\mathrm{fit}} \sqrt{\frac{\mathrm{FilterBandwidth}}{\mathrm{FilterTransmission} \times \mathrm{DetectorResponse} \times \mathrm{LaserPower}^2}} \times \frac{\lambda}{\mathrm{BP}_{\mathrm{factor}}}$$

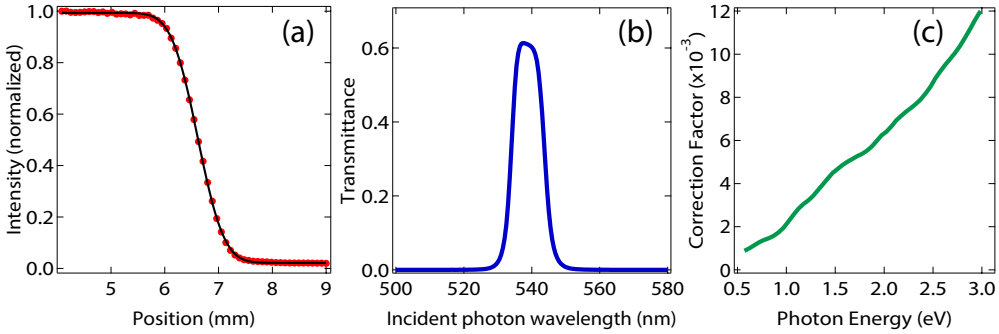

Figure C.1: Various correction factors used to account for wavelength dependent artifacts. (a) Knife-edge measurement to determine beam waist of the incident laser beam at $\lambda = 1100$ nm. (b) Measured transmission coefficient of the bandpass filter centered at 540 nm, and used to measure the data point corresponding to 1080 nm incident wavelength. (c) The Bloembergen-Pershan correction factor as a function of incident photon energy. Figures (a), (b) courtesy of D. Torchinsky, obtained through private communication.

Fits to polar channel data

Although the fitting schemes described in equations 2.4, 2.6, and 2.7 are insufficient to determine the complete relative phase information between the components $|\chi_{\mathrm{zzz}}|$, $|\chi_{\mathrm{zxx}}|$, and $|\chi_{\mathrm{xzx}}|$, we are able to make some definitive statements about the relative phases. Figure C.2d shows a comparison of fits to the data in the vertical channel calculated with assuming that the relative sign between χ_{zxx} and χ_{zzz} is either $(+)$ or $(-)$. The fits clearly prefer a relative $(-)$ sign for the data. This preference is observed to be valid for all incident wavelengths $\lambda > 1100$ nm, whereas for $\lambda < 1100$ nm, the $(+)$ fits are preferred.

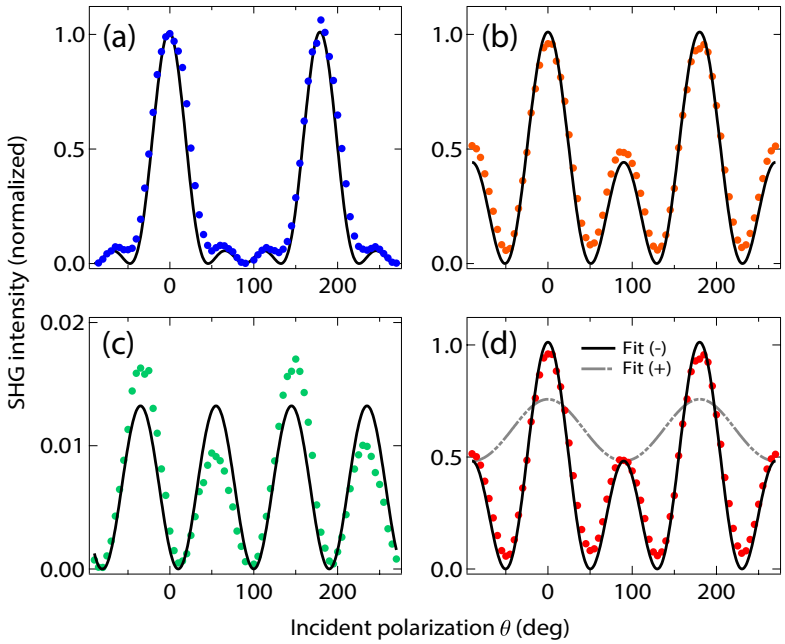

Figure C.2: Minimized mean-squared fits (solid lines) to the experimental data (dots) in three polarization channels (a) *parallel*, (b) *vertical*, and (c) *horizontal* at incident light wavelength $\lambda = 1400$ nm. (d) Comparison of fits to the data in the vertical channel calculated with assuming that the relative sign between χ_{zxx} and χ_{zzz} is either (+) or (−). The fits clearly prefer a relative (−) sign for the data.

Bibliography

[1] Nicolo Accanto et al. "Second harmonic nano-particles for femtosecond coherent control on the nanoscale". In: *arXiv preprint arXiv:1305.3783* (2013).

[2] P. W. Anderson and E. I. Blount. "Symmetry Considerations on Martensitic Transformations: Ferroelectric Metals?" In: *Physical Review Letters* 14.7 (1965), p. 217.

[3] V. I. Belinicher and B. I. Sturman. "Fokker-Planck equation in the absence of detailed balance". In: *Sov. Phys. Usp* 16 (1974), p. 892.

[4] V. I. Belinicher et al. "Theory of photogalvanic effect in ferroelectrics". In: *Ferroelectrics* (1978). ISSN: 15635112. DOI: 10.1080/00150197808237355.

[5] S. Bergfeld and W. Daum. "Second-Harmonic Generation in GaAs: Experiment versus Theoretical Predictions of χxyz(2)". In: *Physical Review Letters* 90.3 (Jan. 2003), p. 036801. DOI: 10.1103/PhysRevLett.90.036801.

[6] N. Bloembergen and P. S. Pershan. "Light Waves at the Boundary of Nonlinear Media". In: *Physical Review* 128.2 (Oct. 1962), pp. 606–622. DOI: 10.1103/PhysRev.128.606.

[7] Lukas Braun et al. "Ultrafast photocurrents at the surface of the three-dimensional topological insulator Bi2Se3". In: *Nature Communications* (2016). ISSN: 20411723. DOI: 10.1038/ncomms13259.

[8] S. Casalbuoni et al. "Numerical studies on the electro-optic detection of femtosecond electron bunches". In: *Physical Review Special Topics - Accelerators and Beams* (2008). ISSN: 10984402. DOI: 10.1103/PhysRevSTAB.11.072802.

[9] D. Côté, J. E. Sipe, and H. M. van Driel. "Simple method for calculating the propagation of terahertz radiation in experimental geometries". In: *Journal of the Optical Society of America B* (2003). ISSN: 0740-3224. DOI: 10.1364/JOSAB.20.001374.

[10] Jerome Extermann et al. "Nano-FROG: Frequency resolved optical gating by a nanometric object". In: *Optics Express* 16.14 (July 2008), p. 10405. DOI: 10.1364/OE.16.010405.

[11] Bradley Ferguson and Xi Cheng Zhang. *Materials for terahertz science and technology*. 2002. DOI: 10.1038/nmat708.

[12] Richard P Feynman, Robert B Leighton, and Matthew Sands. *The Feynman Lectures on Physics, Vol. I: The New Millennium Edition: Mainly Mechanics, Radiation, and Heat*. 2011. ISBN: 9780465024933. DOI: 10.1119/1.1972241.

[13] G. Gallot and D. Grischkowsky. "Electro-optic detection of terahertz radiation". In: *Journal of the Optical Society of America B* (1999). ISSN: 0740-3224. DOI: 10.1364/JOSAB.16.001204.

[14] Elsa Garmire. "Nonlinear optics in daily life". In: *Optics Express* 21.25 (Dec. 2013), p. 30532. DOI: 10.1364/OE.21.030532.

[15] Ryan C. Haislmaier et al. "Large nonlinear optical coefficients in pseudo-tetragonal BiFeO3 thin films". In: *Applied Physics Letters* 103.3 (July 2013), p. 031906. DOI: 10.1063/1.4812978.

[16] S.Y. Hamh et al. "Helicity-dependent photocurrent in a Bi2Se3 thin film probed by terahertz emission spectroscopy". In: *Physical Review B* (2016). DOI: 10.1103/PhysRevB.94.161405.

[17] Peter Hänggi and Fabio Marchesoni. "Artificial Brownian motors: Controlling transport on the nanoscale". In: *Reviews of Modern Physics* (2009). ISSN: 00346861. DOI: 10.1103/RevModPhys.81.387.

[18] Shin-Ming Huang et al. "A Weyl Fermion semimetal with surface Fermi arcs in the transition metal monopnictide TaAs class". In: *Nature Communications* 6 (June 2015), p. 7373. DOI: 10.1038/ncomms8373.

[19] E. L. Ivchenko and S. D. Ganichev. "Ratchet effects in quantum wells with a lateral superlattice". In: *JETP Letters* (2011). ISSN: 0021-3640. DOI: 10.1134/S002136401111004X.

[20] Sheng Ju, Tian-Yi Cai, and Guang-Yu Guo. "Electronic structure, linear, and nonlinear optical responses in magnetoelectric multiferroic material BiFeO3". In: *The Journal of Chemical Physics* 130.21 (June 2009), p. 214708. DOI: 10.1063/1.3146796.

[21] T. H. Kim et al. "Polar metals by geometric design". In: *Nature* 533.7601 (May 2016), pp. 68–72. ISSN: 0028-0836. DOI: 10.1038/nature17628. URL: http://www.nature.com/articles/nature17628.

[22] R. D. King-Smith and David Vanderbilt. "Theory of polarization of crystalline solids". In: *Physical Review B* (1993). ISSN: 01631829. DOI: 10.1103/PhysRevB.47.1651.

[23] Miles V. Klein and Thomas E. Furtak. *Optik*. Springer-Verlag, 2013.

[24] Sergei V. Koniakhin. "Ratchet effect in graphene with trigonal clusters". In: *European Physical Journal B* (2014). ISSN: 14346036. DOI: 10.1140/epjb/e2014-50434-4.

[25] E. J. König et al. "Photogalvanic effect in Weyl semimetals". In: *Physical Review B* (2017). ISSN: 24699969. DOI: 10.1103/PhysRevB.96.075123.

[26] N. Laman, M. Bieler, and H. M. Van Driel. "Ultrafast shift and injection currents observed in wurtzite semiconductors via emitted terahertz radiation". In: *Journal of Applied Physics* (2005). ISSN: 00218979. DOI: 10.1063/1.2131191.

[27] Zhilin Li et al. "Weyl Semimetal TaAs: Crystal Growth, Morphology, and Thermodynamics". In: *Crystal Growth and Design* (2016). ISSN: 15287505. DOI: 10.1021/acs.cgd.5b01758.

[28] B. Q. Lv et al. "Observation of Weyl nodes in TaAs". In: *Nature Physics* (2015). ISSN: 17452481. DOI: 10.1038/nphys3426.

[29] Qiong Ma et al. "Direct optical detection of Weyl fermion chirality in a topological semimetal". In: *Nature Physics* (2017). ISSN: 17452481. DOI: 10.1038/nphys4146.

[30] Robert C. Miller. "Optical Harmonic Generation in Single Crystal BaTi O 3". In: *Physical Review* 134.5A (June 1964), A1313–A1319. DOI: 10.1103/PhysRev.134.A1313.

[31] Takahiro Morimoto and Naoto Nagaosa. "Topological nature of nonlinear optical effects in solids". In: *Science Advances* 2.5 (2016). DOI: 10.1126/sciadv.1501524.

[32] J. J. Murray et al. "Phase relationships and thermodynamics of refractory metal pnictides: The metal-rich tantalum arsenides". In: *Journal of The Less-Common Metals* (1976). ISSN: 00225088. DOI: 10.1016/0022-5088(76)90220-4.

[33] M. C. Nuss and J. Orenstein. "Terahertz Time-Domain Spectroscopy". In: *Terahertz Optoelectronics*. 1998. ISBN: 9783540200130. DOI: 10.1007/10828028{_}7.

[34] P. Olbrich et al. "Classical ratchet effects in heterostructures with a lateral periodic potential". In: *Physical Review B - Condensed Matter and Materials Physics* (2011). ISSN: 10980121. DOI: 10.1103/PhysRevB.83.165320.

[35] Shreyas Patankar et al. "Resonance-enhanced optical nonlinearity in the Weyl semimetal TaAs". In: (Apr. 2018). URL: http://arxiv.org/abs/1804.06973.

[36] Tonatiuh Rangel et al. "Large Bulk Photovoltaic Effect and Spontaneous Polarization of Single-Layer Monochalcogenides". In: *Physical Review Letters* (2017). ISSN: 10797114. DOI: 10.1103/PhysRevLett.119.067402.

[37] Raffaele Resta and David Vanderbilt. "Theory of polarization: A modern approach". In: *Topics in Applied Physics* (2007). ISSN: 03034216. DOI: 10.1007/978-3-540-34591-6{_}2.

[38] M. J. Rice and E. J. Mele. "Elementary excitations of a linearly conjugated diatomic polymer". In: *Physical Review Letters* (1982). ISSN: 00319007. DOI: 10.1103/PhysRevLett.49.1455.

[39] Charles A. Schmuttenmaer. "Exploring dynamics in the far-infrared with terahertz spectroscopy". In: *Chemical Reviews* (2004). ISSN: 00092665. DOI: 10.1021/cr020685g.

[40] Ichiro Shoji et al. "Absolute scale of second-order nonlinear-optical coefficients". In: *Journal of the Optical Society of America B* 14.9 (Sept. 1997), p. 2268. DOI: 10.1364/JOSAB.14.002268.

[41] J. E. Sipe and A. I. Shkrebtii. "Second-order optical response in semiconductors". In: *Physical Review B* 61.8 (Feb. 2000), pp. 5337–5352. DOI: 10.1103/PhysRevB.61.5337.

[42] Richard Lee Sutherland, Daniel Garth McLean, and Sean. Kirkpatrick. *Handbook of nonlinear optics.* 2003. URL: https://www.crcpress.com/Handbook-of-Nonlinear-Optics/Sutherland/p/book/9780824742430.

[43] A. Tomasino et al. "Wideband THz time domain spectroscopy based on optical rectification and electro-optic sampling". In: *Scientific Reports* (2013). ISSN: 20452322. DOI: 10.1038/srep03116.

[44] H. P. Wagner et al. "Dispersion of the second-order nonlinear susceptibility in ZnTe, ZnSe, and ZnS". In: *Physical Review B* 58.16 (Oct. 1998), pp. 10494–10501. DOI: 10.1103/PhysRevB.58.10494.

[45] Zhijun Wang et al. "Time-Reversal-Breaking Weyl Fermions in Magnetic Heusler Alloys". In: *Physical Review Letters* (2016). ISSN: 10797114. DOI: 10.1103/PhysRevLett.117.236401.

[46] Liang Wu et al. "Giant anisotropic nonlinear optical response in transition metal monopnictide Weyl semimetals". In: *Nature Physics* 13.4 (Apr. 2017), pp. 350–355. DOI: 10.1038/nphys3969.

[47] Q. Wu and X. C. Zhang. "Ultrafast electro-optic field sensors". In: *Applied Physics Letters* (1996). ISSN: 00036951. DOI: 10.1063/1.115665.

[48] Su Yang Xu et al. "Discovery of a Weyl fermion semimetal and topological Fermi arcs". In: *Science* (2015). ISSN: 10959203. DOI: 10.1126/science.aaa9297.

[49] Su Yang Xu et al. "Observation of Fermi arc surface states in a topological metal". In: *Science* (2015). ISSN: 10959203. DOI: 10.1126/science.1256742.

[50] Steve M. Young and Andrew M. Rappe. "First Principles Calculation of the Shift Current Photovoltaic Effect in Ferroelectrics". In: *Physical Review Letters* 109.11 (Sept. 2012), p. 116601. DOI: 10.1103/PhysRevLett.109.116601.

[51] Cheng Long Zhang et al. "Signatures of the Adler-Bell-Jackiw chiral anomaly in a Weyl fermion semimetal". In: *Nature Communications* (2016). ISSN: 20411723. DOI: 10.1038/ncomms10735.